The Astrophysical Journal, 660:346 – 362, 2007 May 1

A MULTIWAVELENGTH STUDY OF M17: THE SPECTRAL ENERGY DISTRIBUTION AND PAH EMISSION MORPHOLOGY OF A MASSIVE STAR FORMATION REGION

Matthew S. Povich,[1] Jennifer M. Stone,[1] Ed Churchwell,[1] Ellen G. Zweibel,[1] Mark G. Wolfire,[2]
Brian L. Babler,[1] Rémy Indebetouw,[3] Marilyn R. Meade,[1] and Barbara A. Whitney[4]
Received 2006 December 15; accepted 2007 January 20

ABSTRACT

We combine diffuse emission photometry from GLIMPSE and several other Galactic plane surveys covering near-IR through radio wavelengths to synthesize a global spectral energy distribution (SED) for the M17 complex. By balancing the integrated flux in the SED with the total bolometric luminosity of all known O and early B stars in the ionizing cluster, we estimate a distance to M17 of $1.6^{+0.3}_{-0.1}$ kpc. At this distance, the observed total flux in the SED corresponds to a luminosity of $2.4 \pm 0.3 \times 10^6\ L_\odot$. We find that the SED from the H II region peaks at shorter wavelengths and has a qualitatively different shape than the SED from the photodissociation region (PDR). We find that polycyclic aromatic hydrocarbons (PAHs) are destroyed over a short distance or edge at the boundary of the H II region. We demonstrate that this PAH destruction edge can be located easily using GLIMPSE band-ratio images and confirm this using *Spitzer* IRS spectra. We investigate the relative roles of extreme ultraviolet (EUV) and X-ray photons in the destruction of PAHs, concluding that X-rays are not an important PAH destruction mechanism in M17 or, by extension, in any other Galactic H II region. Our results support the hypothesis that PAHs are destroyed by EUV photons within H II regions. PAHs dominate the mid-IR emission in the neutral PDR beyond the ionized gas.

Subject headings: dust, extinction — H II regions — infrared: ISM — radio continuum: ISM — stars: formation — X-rays: ISM

1. INTRODUCTION

M17, the Omega Nebula [W38 at $(l,\ b) = (15.1^\circ,\ -0.7^\circ)$], is a premier example of a young, massive star formation region in the Galaxy. It has a rich observational literature that spans nearly two centuries. Felli et al. (1984; hereafter FCM84) summarized the infrared (IR) and radio observations of M17 up to 1984. A more recent review of the M17 literature and discussion of its properties is given by Townsley et al. (2003, hereafter T03). Although not the most luminous H II region in the Galaxy, M17 is one of the brightest IR and thermal radio sources in the sky, comparable to the nearby Orion Nebula (Orion A). M17 is 4 times more distant from the Sun than Orion and considerably more energetic. The M17 H II region is ionized by the open cluster NGC 6618, which contains over 100 OB stars (Lada et al. 1991) and has an age of less than 3 Myr (Jiang et al. 2002). The center of the cluster is dominated by a ring of seven O stars $1'$ in diameter (Hanson et al. 1997). NGC 6618 contains at least four O stars earlier than O6 V, the spectral type of θ^1 Ori C, the most luminous star in the Trapezium cluster in Orion. The stars in the central part of the NGC 6618 cluster lie behind an average extinction of $A_V = 8$, but in many parts of M17 the extinction is considerably higher, with $A_V > 20$ (Hanson et al. 1997). Because its complex extinction varies with both position and wavelength, M17 is optically bright but much more brilliant in the IR, and the morphology of the extended emission is highly dependent on the wavelength observed. The underlying structure of the radio H II region is divided into two parts, usually called the northern and southern bars, lying on either side of the star cluster (see Fig. 1 for a large-scale view of M17). The two bars with their respective photodissociation regions (PDRs) meet each other at an apparent angle of about 45°, forming an inverted V shape as viewed in Galactic coordinates, with the V opening away from the Galactic midplane. Although only the northern bar is observable at optical wavelengths (in Hα, for example), the southern bar contains the majority of the mass and current star formation activity, including the ultracompact (UC) H II region M17-UC1 (FCM84), the bright IR source M17 SW-IRS (also called the "Kleinmann-Wright object"; Kleinmann & Wright 1973), and numerous young stellar objects (YSOs; Nielbock et al. 2001). Hence, the southern bar and PDR are considerably brighter than the northern bar at mid-IR to radio wavelengths.

The M17 H II region is erupting from the side of the giant molecular cloud M17 SW, and the southern bar marks the primary interface between the ionization edge (I-front) of the H II region and the molecular gas (Lada 1976; FCM84). The entire H II region is expanding, with the southern bar gradually eating into the side of the molecular cloud while the northern bar is pushed outward in the opposite direction (Tsivilev & Krasnov 1999; Pellegrini et al. 2007). The physical processes shaping M17 are analogous to those operating in the Orion Nebula, but the nearly edge-on orientation of the I-front in the southern bar of M17 facilitates the detailed study of the interaction between the H II region, PDR, and molecular cloud (FCM84; Meixner et al. 1992; Chrysostomou et al. 1992; Créte et al. 1999). The entire M17 H II region can be regarded as an energetic interstellar bubble blown into the surrounding interstellar medium (ISM) by the action of the combined winds of the OB stars (Weaver et al. 1977 ; Koo & McKee 1992; Capriotti & Kozminski 2001). The region between the two bars has been almost completely evacuated; T03 observed that superheated ($T \sim 10^7$ K) X-ray-emitting plasma fills the cavity and exits at the eastern opening (toward negative Galactic latitudes) as a "champagne

[1] Department of Astronomy, University of Wisconsin, Madison, WI 53706; povich@astro.wisc.edu.
[2] Department of Astronomy, University of Maryland, College Park, MD 20742-2421.
[3] Department of Astronomy, University of Virginia, Charlottesville, VA 22903-0818.
[4] University of Colorado, Space Science Institute, Boulder, CO 80303-1012.

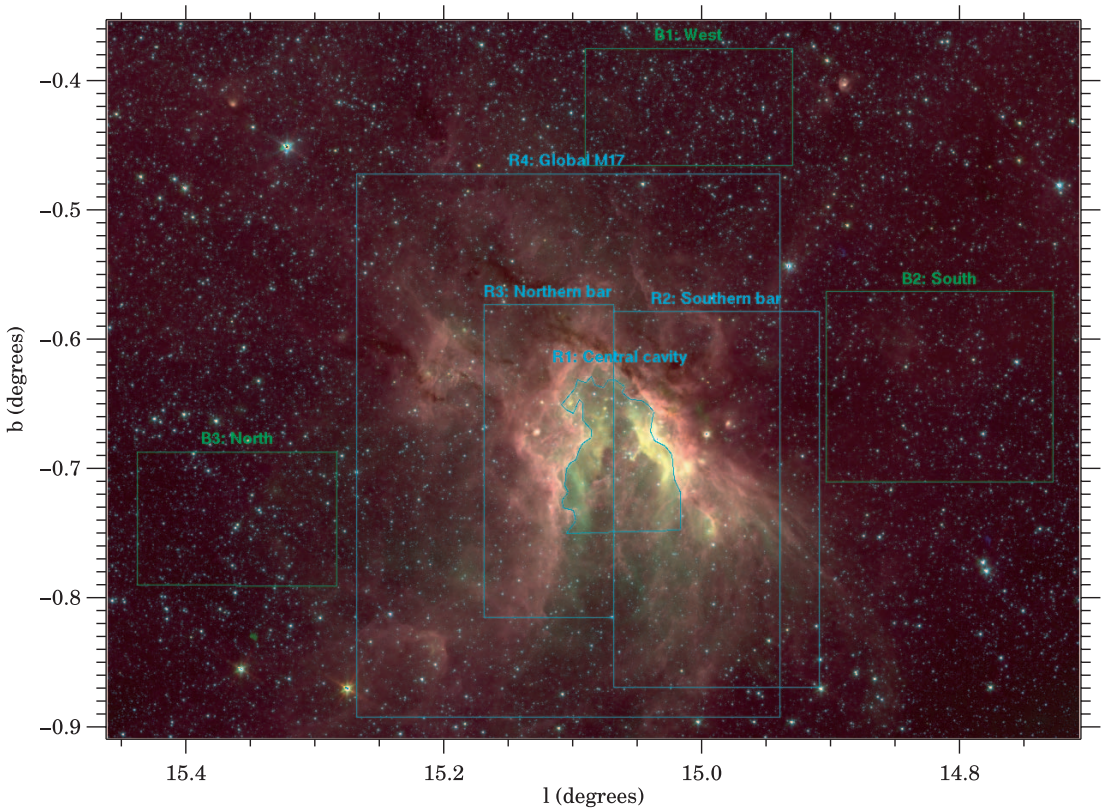

FIG. 1.—Apertures (*cyan*) used to extract diffuse fluxes overplotted on a three-color (*red*: 5.8 μm; *green*: 4.5 μm; *blue*: 3.6 μm) GLIMPSE image mosaic of the M17 region. The green boxes enclose areas used to determine the background levels. Point-source-subtracted residual images were used for the GLIMPSE diffuse photometry. The northern and southern bars are named after their orientation with respect to equatorial coordinates; this image is displayed in Galactic coordinates.

flow" energized by multiple shocks from colliding OB winds. Hence, M17 is an extremely energetic example of the class of interstellar bubbles associated with massive star formation regions cataloged in the Galactic Legacy Infrared Mid-Plane Survey Extraordinaire (GLIMPSE) by Churchwell et al. (2006), although M17 was not selected for the GLIMPSE bubbles catalog due to its peculiar, V-shaped morphology. M17 is also considered a prime candidate site for sequential or stimulated star formation (Elmegreen & Lada 1976). The NGC 6618 cluster members appear to be recently emerged from their natal dust envelopes, while the bars contain populations of heavily embedded YSOs (Lada et al. 1991; Hanson et al. 1997; Jiang et al. 2002), suggesting a differentiation in age across the complex. Following the initial wave of star formation that produced the ionizing cluster, the expansion of the H II region drives the southern bar into M17 SW, compressing it and possibly inducing marginally stable protostellar cores to collapse.

M17 has been studied extensively over a wide range of wavelengths, and due to its location near the Galactic midplane it has been observed as part of multiple Galactic plane surveys from the near-IR to radio. We have made use of new and archival image mosaics of M17 from GLIMPSE, the Two-Micron All-Sky Survey (2MASS; Skrutskie et al. 2006), the *Midcourse Space Experiment* (*MSX*; Price et al. 2001) Galactic Plane Survey, the *IRAS* Sky Survey Atlas (ISSA),[5] and the Multi-Array Galactic Plane Imaging Survey (MAGPIS; Helfand et al. 2006) to synthesize a multiwavelength picture of the global diffuse emission characteristics of M17. The high mid-IR resolution and sensitivity provided by the Infrared Array Camera (IRAC) on the *Spitzer Space Telescope* allow us to map the structures of the H II region and PDRs in unprecedented detail using image mosaics from GLIMPSE. In particular, we can trace the transition between the I-front and the PDR that is outlined by emission generally attributed to polycyclic aromatic hydrocarbon (PAH) molecules. Complementary spectra from the *Spitzer* Infrared Spectrograph (IRS) provide evidence of the changing ionization state of the gas and the emergence of PAH emission features, supporting our interpretation of the GLIMPSE images. We summarize the various data sets used in this study in § 2, and we discuss our aperture photometry and construction of a global spectral energy distribution (SED) for M17 in § 3. Analysis of the PAH emission morphology and the role of extreme ultraviolet (EUV) photons and possibly X-rays in destroying PAH molecules are presented in § 4. Our conclusions are summarized in § 5.

2. THE DATA

2.1. *GLIMPSE and 2MASS*

M17 is the brightest large (>10′ in extent) source of diffuse mid-IR emission in the entire GLIMPSE survey area ($|l| = 10°–65°$, $|b| \leq 1°$; Benjamin et al. 2003). This survey imaged the Galaxy using the four bands of *Spitzer* IRAC, centered at 3.6, 4.5, 5.8, and 8.0 μm with corresponding bandwidths of 0.75, 1.0, 1.4, and 2.9 μm (Fazio et al. 2004). High-resolution (1.2″ pixels) image mosaics were created by the GLIMPSE pipeline[6] from Basic Calibrated Data (BCD) image frames processed by the Spitzer Science Center (SSC). The GLIMPSE pipeline removes

[5] Go to http://irsa.ipac.caltech.edu/IRASdocs/issa.exp.sup.

[6] Details of the data processing can be found at http://www.astro.wisc.edu/glimpse/docs.html.

artifacts such as stray light (all bands), muxbleed ([3.6] and [4.5] bands), and banding ([5.8] and [8.0] bands).[7] The SSC Mopex package was used to mask image artifacts (primarily cosmic rays) and the IPAC Montage package was used to mosaic the images. Mosaics produced from 2MASS (Skrutskie et al. 2006) data provide complementary images to GLIMPSE in the near-IR JHK_S bands.

A modified version of Daophot (Stetson 1987) was used to extract point sources detected at greater than the 2 σ level from the GLIMPSE and 2MASS image frames. Daophot creates residual images of the GLIMPSE images with the point sources removed. These residual frames were mosaicked in Montage to produce large-area residual image mosaics. The residuals, intended for photometry of diffuse or extended emission, are the GLIMPSE image mosaics with the point sources removed and saturated pixels masked out. The positions and fluxes of extracted point sources detected at greater than 3 σ in any of the 4 GLIMPSE bands are entered into the GLIMPSE Full List of point sources, of which the Point Source Archive (sources detected at greater than 5 σ in any two GLIMPSE bands) and the 99.5% reliable GLIMPSE Point Source Catalog are subsets. For the purposes of this study, we utilize both the GLIMPSE and 2MASS mosaics and GLIMPSE residual image mosaics of M17, supplemented by GLIMPSE and 2MASS point-source fluxes from the Full List.

2.2. *MSX*

The Spirit III instrument on board the *MSX* satellite surveyed the Galactic plane in four IR bands (Price et al. 2001): A (isophotal wavelength 8.28 μm, $\gtrsim$50% peak intensity 6.8–10.8 μm), C (12.13 μm, 11.1–13.2 μm), D (14.65 μm, 13.5–15.9 μm), and E (21.3 μm, 18.2–25.1 μm). The spatial resolution of this instrument was $\sim$18.3″, and we use cutout images of M17 from the NASA/IPAC Infrared Science Archive (IRSA)[8] that have 6″ pixels. Although its resolution and sensitivity are inferior to that of *Spitzer*, the absolute flux calibration of *MSX*, determined in-flight by measuring the fluxes from projectiles fired away from the spacecraft, is reliable to $\sim$1% (Price et al. 2004). Hence *MSX* mid-IR fluxes are the most accurate currently available, providing the benchmark against which IRAC [8.0] fluxes can be compared (Cohen et al. 2007). The lower sensitivity of *MSX* is advantageous in studying M17, because this region is extremely bright in diffuse IR emission. The *MSX* images do not saturate in any of the four bands, while the IRAC [8.0] image is saturated in the brightest part of the SW bar, and the 24 μm image from the Multiband Imaging Photometer for *Spitzer* Galactic Plane Survey (MIPSGAL; Carey et al. 2006) is completely saturated over the entire M17 H II region.

2.3. *IRAS*

From January to November 1983 the *Infrared Astronomy Satellite* (*IRAS*) mapped 98% of the sky in four broad IR bands. These bands have effective wavelengths of 12, 25, 60, and 100 μm with bandwidths of 6.5, 11, 40, and 37 μm, respectively (Beichman et al. 1988). Although the sensitivity of *IRAS* was comparable to that of *MSX*, its resolution was much lower, and the ISSA cutout images[9] have 1.5′ pixels.

2.4. *MAGPIS Radio Continuum*

The MAGPIS project, described by Helfand et al. (2006) is a compilation of high-resolution images spanning the Galactic plane from the Very Large Array (VLA) and complementary IR surveys. Cutouts from available images can be downloaded from the MAGPIS Web site.[10] M17 is included in the VLA New Galactic Plane Survey (New GPS) at 20 cm and the GPS at 90 cm. The 20 cm images combine data from the B, C, and D configurations of the VLA with data from the Effelsberg 100 m telescope, resulting in high-resolution images (2″ pixel sizes, with $6.2'' \times 5.4''$ half-power restoring beamwidth) that do not suffer from the usual interferometric loss in flux. The 90 cm images were produced from VLA maps in the B and C configurations.

2.5. *Spitzer IRS Spectra*

Spitzer IRS observations were obtained as part of program ID 3697 (PI: M. Wolfire), to map the PDR in M17 SW in the IRS SH (short-high) and LH (long-high) modules (Houck et al. 2004). In this work, we make use of the SH pointings, covering the wavelength range of 9.9–19.6 μm with a spectral resolution of $\sim$600. The observations consist of 11 sets of SH astronomical observation requests (AORs), each with 12 one-half slit steps (5.6″) in the slit-parallel direction and 4 full slit steps (4.7″) in the slit-perpendicular direction. The integration time was 6 s per position. The first AOR was carried out in 2004 October and the remaining 10 in 2005 April. The BCDs have been processed with the SSC pipeline IRS 13.2.

3. SED AND ENERGY BALANCE

3.1. *Aperture Photometry*

To construct multiwavelength SEDs of M17, we performed aperture photometry on images from each of the near- through mid-IR bands, using point-source subtracted images where appropriate. We extracted submosaics from each of the apertures shown superimposed on a three-color (*red*: 5.8 μm; *green*: 4.5 μm; and *blue*: 3.6 μm) GLIMPSE mosaic of the M17 region in Figure 1. The diffuse emission morphology of M17 is very complex, yet we chose mainly box-shaped apertures for ease of extraction. We are able to use this simple scheme because M17 is extremely bright relative to the IR background in the Galactic plane, and we are interested only in large-scale integrations of the flux from different parts of the nebula, as well as the "global" flux from the entire nebula. Aperture R1 was chosen to extract emission dominated by the H II region. Our target apertures range in size from $\sim 4' \times \sim 6'$ (R1) to $16.4' \times 21.1'$ (box R4). We measured the flux in each of the background apertures (B1, B2, and B3) and used a weighted average of the measured fluxes to compute a background level, B (Jy pixel^{-1}), for each IR band. We integrated the intensity images (MJy sr^{-1}) over each target aperture (R1, R2, R3, and R4) and converted these values to flux F_0 (Jy). The background-subtracted fluxes were then calculated for each aperture as

$$F = F_0 - Bn_{\rm pix}, \quad (1)$$

where $n_{\rm pix}$ is the number of pixels contained within the aperture.

The above procedure was carried out on the GLIMPSE residual images for IRAC [3.6], [4.5], and [5.8] that are free of the pollution of point sources and on the *MSX* and *IRAS* images. The lower resolution and sensitivity of *MSX* and *IRAS* precludes the removal of the majority of the point sources detected by

[7] See the *Spitzer* Observer's Manual at http://ssc.spitzer.caltech.edu/documents/som for definitions of the various IRAC image artifacts.

[8] See http://irsa.ipac.caltech.edu/Missions/msx.html.

[9] See http://irsa.ipac.caltech.edu/Missions/iras.html.

[10] See http://third.ucllnl.org/gps.

GLIMPSE. Fortunately, in a region like M17 the brightness of diffuse IR emission increases sharply with wavelength, while the total flux in stars (the majority of which are field stars, not YSOs) decreases. In IRAC [5.8], the total flux of all point sources included in the Full List (see § 2.1) from the M17 bars is less than 1% of the diffuse flux measured from the residual image. When treating the *MSX* and *IRAS* bands it is therefore safe to neglect the contribution of point sources.

The 2MASS near-IR bands are stellar-dominated over most of the GLIMPSE survey area, and therefore no residual images are made of the 2MASS mosaics. A portion of the southern bar of M17 near M17-UC1 is bright enough in diffuse emission to reach the nonlinear saturation limit of 4.0 mag[11] for IRAC [8.0], and this part of the residual image is heavily masked as a result. We therefore use a modified version of our aperture photometry scheme to obtain the diffuse fluxes in the JHK_S and [8.0] bands. We measure fluxes in each aperture directly from the mosaics, which include stars, and then determine the diffuse flux values for F_0 and B used in equation (1) by subtracting the total flux from all point sources in the corresponding aperture area of the Full List from the total flux (diffuse and stellar) in the mosaic. Because both the mosaics and residual images have the same flux calibration, for a given aperture the flux in the mosaic image should agree with the flux in the residual image plus the total flux of all extracted point sources. Although the [8.0] flux will still be underestimated using this procedure, for the construction of a global SED it is preferable to include flux from saturated pixels than to exclude these pixels completely. There is a possible disparity between these two procedures due to the small gap between the 2 σ detection level of sources extracted from the residual image and the 3 σ minimum level of sources included in the Full List. As a check, comparison of these two methods, carried out for the same set of apertures in IRAC [3.6], [4.5], and [5.8] (for which we have both mosaics and good residual images of M17), shows that the results agree to within a few percent. All of our diffuse fluxes are formally upper limits because there is an irreducible contribution from unresolved or otherwise unextracted point sources in all of the bands. In practice, however, the background subtraction partially offsets the potential systematic contribution of unextracted point sources, and our conservative estimates of the uncertainties on our measured fluxes accounts for any remaining effect.

We estimate the uncertainties on our measured IR fluxes primarily from the background levels, incorporating the total fluxes of point sources, $F_\star$, subtracted from the mosaic fluxes in JHK_S and [8.0]. Hence, our fractional uncertainties are given by

$$\frac{\delta F}{F} = \left[\left(\frac{B n_{\rm pix}}{F_0} \right)^2 + \left(0.2 \frac{F_\star}{F_0} \right)^2 \right]^{1/2}, \quad (2)$$

which becomes simply

$$\frac{\delta F}{F} = \frac{B n_{\rm pix}}{F_0}$$

when point-source fluxes are not used ($F_\star = 0$). We made every attempt to be conservative with these uncertainty estimates. Typical percentage uncertainties on our global fluxes (aperture R4) for M17 are 50% at K_S (where background levels are high and unresolved stellar emission is a significant source of contamination to the diffuse emission), <30% for the GLIMPSE bands, ~5% for *MSX*, and 5%–27% for *IRAS* 12–100 μm. For the other, smaller apertures where the diffuse emission is brighter on average, the uncertainties are lower.

Additional sources of systematic error affect the absolute diffuse flux calibrations of IRAC images. Cohen et al. (2007) compared the fluxes measured by IRAC at 8.0 μm and *MSX* at 8.3 μm for a sample of 43 Galactic H II regions and found, correcting for the difference in the bandpasses, that the present calibration of IRAC [8.0] tends to overestimate diffuse fluxes by 36%. This problem is believed to be due to scattered light inside the camera and therefore should similarly affect IRAC [5.8]. Because there are no *MSX* bands lying close to the 3 lower wavelength IRAC bands, aperture correction factors have been estimated for all four bands using extragalactic SED templates. The two approaches agree well for IRAC [8.0]. We therefore adopt the SSC "infinite-aperture" correction factors determined by Jarrett[12] and multiply our flux values at 3.6, 4.5, 5.8, and 8.0 μm by factors of 0.91, 0.94, 0.73, and 0.74, respectively. There is an additional source of systematic error caused by "full-frame pull-up" (also called "droop") whereby the flux of a bright source can be redistributed across the IRAC detector, raising the diffuse emission everywhere within the affected image frame. Droop is evident in many GLIMPSE mosaics, especially at 8.0 μm, where a frame containing a bright compact source appears brighter than adjacent frames. The causes of droop are not well-understood, and at present there is no way to fully correct for this effect, but since M17 extends over a large area containing many individual IRAC frames, any redistributed diffuse flux is likely to be counted as part of the global SED.

The *IRAS* flux calibration has been checked against *COBE* DIRBE (Hauser et al. 1991) and a linear transformation of the form

$$F_{\rm cor} = {\rm Gain} \times F + {\rm Offset} \quad (3)$$

to correct the *IRAS* fluxes has been derived.[13] We apply these transformations to our measured *IRAS* fluxes, with the caveat that the correction is most valid at angular scales comparable to the 1° resolution of DIRBE. The uncertainties on the correction constants (gain and offset) are propagated into our final uncertainty estimates. Finally, the breadth of the *IRAS* bands necessitates the application of color-corrections to the isophotal fluxes (Beichman et al. 1988). We chose color-correction factors based on a blackbody SED model determined from the observed ratio of 60 to 100 μm fluxes. For M17, the color-corrections primarily affect the 12 and 25 μm fluxes; the 60 and 100 μm fluxes are largely unchanged. The combined effect of the *IRAS* flux transformations and color-corrections is to decrease the flux values at 12, 60, and 100 μm by ~5%, ~20%, and ~35%, respectively, while increasing the flux at 25 μm by ~17%.

We use the same apertures to extract the integrated radio continuum fluxes from the VLA MAGPIS images at 20 cm and 90 cm. In this case, background subtraction is inappropriate, and the images, while probably not missing significant flux, were not intended for photometric applications. In addition, part of the M17 H II region extends beyond the edge of the New GPS survey, and consequently the 20 cm image of M17 is slightly cropped in our largest apertures. We estimate this causes a loss of not more than 5% of the continuum flux, based on the very low extrapolated brightness of the missing portions compared with the peak brightness observed. Hence, we use the MAGPIS data with caution,

[11] Go to http://www.astro.wisc.edu/glimpse/GQA-master.pdf.

[12] Go to http://ssc.spitzer.caltech.edu/irac/calib/extcal.

[13] See http://irsa.ipac.caltech.edu/IRASdocs/issa.exp.sup/ch4/D.html.

TABLE 1
M17 Integrated Diffuse Infrared Fluxes (Jy)

Band	λ (μm)	Bandwidth (μm)	Aperture R1		Aperture R2		Aperture R3		Aperture R4	
			F_1	δF_1	F_2	δF_2	F_3	δF_3	F_4	δF_4
2MASS *J*	1.25	0.16	37	3	28	10	29	6	46	23
2MASS *H*	1.65	0.25	45	5	30	15	32	10	31	23
2MASS K_S	2.17	0.26	80	6	79	25	66	14	113	56
IRAC 1	3.6	0.75	110	10	240	50	200	30	540	210
IRAC 2	4.5	1.0	170	10	290	40	220	20	620	140
IRAC 3	5.8	1.4	500	60	1300	300	1100	200	2900	1100
IRAC 4 obs.[a]	8.0	2.9	3000	200	5000	1000	4200	550	11,000	3800
IRAC 4 pred.[b]	8.0	2.9	4480	170	5600	500	4480	360	11,500	600
MSX A	8.28	4.0	4000	100	5000	400	4000	300	10,300	500
IRAS	12	5.5	6300[c]	200	5700	400	5000	300	11,000	1200
MSX C	12.13	2.1	13,500	200	14,600	1000	10,700	600	27,500	1400
MSX D	14.65	2.4	22,100	100	21,300	600	14,500	300	37,700	1900
MSX E	21.30	6.9	52,400	200	59,700	1000	39,000	500	105,000	5000
IRAS	25	11	48,100[c]	1000	60,300	1900	37,100	1000	110,000	4800
IRAS	60	40	49,000[c]	3700	98,000	11,000	75,000	6400	230,000	30,000
IRAS	100	37	39,800[c]	6300	86,000	20,000	59,000	11,000	195,000	53,000

[a] Because IRAC [8.0] saturates in the brightest parts of M17, the observed fluxes given here are underestimates of the actual emission, particularly for apertures R1 and R2.
[b] IRAC [8.0] fluxes predicted using the ratio of IRAC[8.0]/*MSX A* $= 1.12 \pm 0.03$ derived by Cohen et al. (2007) for a typical bright H II region SED.
[c] The resolution of *IRAS* ($\sim$0.5′ at 12 μm to $\sim$2′ at 100 μm; Beichman et al. 1988) is too coarse to allow a precise extraction of flux from R1; therefore, the *IRAS* fluxes for this aperture are only in approximate spatial correspondence with the other fluxes listed.

assigning error bars of 30%, but it is possible to check our results. The thermal radio continuum of M17 has been measured previously using single-dish radio observations. Schraml & Mezger (1969) give 609 Jy at 1.95 cm and Goss & Shaver (1970) give 794 Jy at 6 cm. Our value of 687 Jy for the MAGPIS 20 cm is consistent with these older measurements. No uncertainty estimates are given for these published fluxes, so we also assign them 30% error bars. Several other continuum flux measurements for M17 are quoted in the literature. The fluxes measured by Altenhoff et al. (1970) at 2, 6, and 20 cm, all under 600 Jy, appear to be systematically underestimated. Downes et al. (1980) give a flux of 844.5 Jy at 6 cm, but this is a rough estimate derived from the peak flux assuming that the source is Gaussian, a poor assumption for a region as complex as M17. The radio continuum fluxes that we use for this work have been independently determined at three different frequencies, and all are in good relative agreement.

3.2. *The Shapes of the SEDs*

The measured integrated IR fluxes with their uncertainties for our four apertures on M17 are given in Table 1. Conti & Crowther (2004) measured the diffuse IR fluxes for M17 in the *MSX* C and E bands and in all the *IRAS* bands except 12 μm. Their values of 22,400 and 89,100 Jy at 12.13 and 21.30 μm, respectively, agree well with our determinations of *MSX* fluxes, adjusting for the smaller size of their 9′ circular aperture relative to our most comparable combination of apertures, R2+R3. Their *IRAS* fluxes of 83,200, 214,000, and 224,000 Jy at 25, 60, and 100 μm resemble our uncorrected *IRAS* fluxes but differ significantly from our final values, after the cross-calibration with DIRBE and color corrections are performed. Conti & Crowther (2004) do not report applying any calibration or color corrections to their *IRAS* fluxes.

We constructed SEDs using the IR flux values of Table 1 along with the radio continuum fluxes at 1.95 cm (Schraml & Mezger 1969), 6 cm (Goss & Shaver 1970), 20 cm, and 90 cm. The SEDs from different combinations of apertures are presented in Figures 2. Figure 2*a* illustrates the shape of the global SED. It is qualitatively similar to the SED of a dust cocoon surrounding a single newly formed early type star (Churchwell et al. 1990; Vig et al. 2006). The underlying shape of the global IR SED resembles a blackbody curve that peaks near 60 μm. This is a "graybody" composite of many underlying dust blackbodies, representing a large range of grain temperatures and sizes found throughout the M17 region. The radio emission from 1.95–20 cm is the approximately flat, thermal bremsstrahlung (free-free) continuum from electrons in the H II region, and it is optically thick at longer wavelengths, as evidenced by the lower flux at 90 cm. The dust continuum rises steeply from near-IR through mid-IR wavelengths. Figure 2*b* compares the IR SED of the H II region surrounding NGC 6618 (aperture R1; *red*), with that of the two PDR bars excluding the H II region (apertures R2+R3-R1; *blue*). The total SED of R2+R3 is reproduced for reference (*green dashed line*); the break in the line spans the silicate feature at 9.7 μm for which we have no observational coverage. The SED from the H II region has a steeper mid-IR continuum and peaks at a shorter wavelength ($\lambda_{\rm peak} \sim 24$ μm) than the SED from the PDRs ($\lambda_{\rm peak} \sim 60$ μm). This is an indication that the grain population inside the H II region is at higher temperatures and probably has a smaller size distribution (Giard et al. 1992) compared to the dust in the PDRs. Figure 2*b* also illustrates the relative contributions of the PAH emission features to the IRAC and *MSX* bands both within the H II region and the PDRs. IRAC [3.6], [5.8], and [8.0] all contain strong PAH emission features and, in the PDR SED, show marked flux excesses relative to IRAC [4.5], which does not include any PAH emission feature. These excesses largely disappear in the H II region SED, although there is some PAH emission in aperture R1, primarily coming from the front and back walls of the cavity. The 2MASS JHK_S fluxes are much higher from inside the H II region than outside. The diffuse near-IR emission is probably dominated by scattered starlight, augmented by free-bound emission from the Paschen and Brackett ionization edges that fall within the J and K_s bands, respectively.

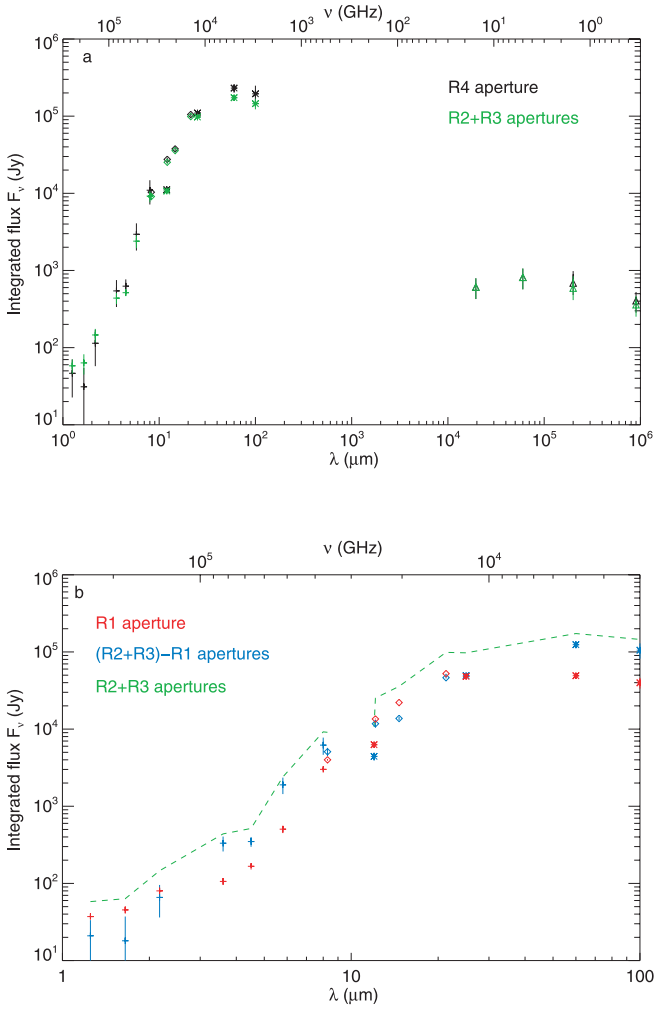

FIG. 2.—Integrated diffuse SEDs for M17. Infrared fluxes and error bars from Table 1 are plotted: 2MASS+GLIMPSE (*plus signs*), *MSX* (*diamonds*), and *IRAS* (*asterisks*). Radio continuum points from Goss & Shaver (1970) Schraml & Mezger (1969) and MAGPIS are plotted as triangles. (*a*) The fluxes from the largest-area aperture, R4 (*black*), represent the "global" SED of M17, while the sum of the fluxes from apertures R2+R3 (*green*) captures the total emission from the two bars and central cavity. The underlying shape of the IR SED is thermal (blackbody) emission from dust. The thermal (free-free) radio continuum is approximately flat from 2–20 cm, falling off by 90 cm. (*b*) Comparison of the IR-only SED from the H II region (*red*) with the PDR (*blue*) shows that the IR emission peaks at shorter wavelengths for dust that lies closer to the ionizing cluster. The *red* and *blue* points sum to the SED of the R2+R3 apertures, reproduced from (*a*) as a green dashed line. The break in the line spans the silicate absorption feature near 10 μm, for which we have no data.

The IRAC [4.5] band, while free of PAH emission, contains one potentially strong emission feature from H II regions, the H I Brα recombination line at 4.05 μm. The emissivity of the Brα line is related to the specific free-free emissivity by

$$\frac{j(\mathrm{Br}\alpha)}{j_\nu(\mathrm{ff})} = 3.058\times10^{12}\left(\frac{T_e}{10^4\ \mathrm{K}}\right)^{0.35}\left(\frac{\nu}{15\ \mathrm{GHz}}\right)^{0.1}\ (\mathrm{Hz}). \quad (4)$$

We evaluate this ratio using an electron temperature $T_e = 8000$ K (Subrahmanyan & Goss 1996). We then calculate the specific flux level of the Brα emission line distributed across the broad IRAC [4.5] band as

$$F_\nu(\mathrm{Br}\alpha) = \frac{j(\mathrm{Br}\alpha)}{j_\nu(\mathrm{ff})}\frac{F_\nu(\nu)}{\Delta\nu}, \quad (5)$$

TABLE 2

Brα LINE EMISSION FROM FREE-FREE RADIO CONTINUUM

Aperture	ν (GHz)	F(ff) (Jy)	F(4.5) (Jy)	F(Brα) (Jy)	Brα (%)
(R4).....	15	609	620	115	19
	5	784	620	133	21
	1.5[a]	687	620	103	17
(R1).....	1.5[a]	257	170	38	22
(R2 + R3 − R1).....	1.5[a]	334	340	50	15

[a] The MAGPIS 20 cm fluxes are slightly underestimated for apertures R2, R3, and R4 because the image is clipped. It is also possible that the free-free emission is optically thick at 20 cm. For these reasons, the continuum fluxes at 1.5 GHz and the Brα line fluxes derived from them are lower limits.

where $F_\nu(\nu)$ is the free-free continuum flux measured at radio frequency ν and $\Delta\nu = 1.5\times10^{13}$ Hz is the IRAC [4.5] bandwidth. The results of these calculations using the radio continuum fluxes at 1.95, 6, and 20 cm are given in Table 2. Comparison of F_ν(Brα) with the fluxes in the IRAC [4.5] band, F_ν(4.5 μm), for various apertures from Table 1, reveals that, on average, the Brα emission line contributes ~20% of the flux at 4.5 μm. It is reasonable to hypothesize a higher fractional contribution of Brα if we examine only the emission from the heart of the H II region compared to the emission from the PDRs largely excluding the H II region. Table 2 includes estimates of F_ν(Brα) based on the 20 cm flux from aperture R1 alone and the combination of apertures R2 + R3 − R1 (see Fig. 2*b*). The contribution of Brα to the 4.5 μm flux in aperture R1 is 22%. This value is not significantly higher than the estimates for the entire R4 aperture, but the percentage Brα contribution in R2+R3−R4, calculated from the 20 cm data, is only 15%. We could be underestimating the Brα emissivity if the free-free emission becomes optically thick at 20 cm. The free-free emissivity is not precisely flat; it rises toward lower frequencies as $j_\nu(\mathrm{ff}) \propto \nu^{-0.1}$, yet the measured flux at 20 cm falls slightly below the flux at 6 cm. This optical depth effect is unlikely to be large on the whole, but it could manifest itself most noticeably in the brightest part of the H II region, causing us to underestimate the degree of enhancement to the Brα line emission there. Taken together, these results indicate that the Brα line emission appears to have a similar spatial distribution to that of the dust graybody continuum, but there is a marginally significant strengthening of the Brα line relative to the dust continuum in the central parts of the H II region. The globally integrated [4.5] diffuse emission is dominated by the central part of the H II region.

3.3. *The Luminosity Distance to M17*

Another view of the global SED of M17 is presented in Figure 3. Plotting the fluxes in λF_λ space shows that the energy radiated in the IR is the dominant source of luminosity, far more important than the energy radiated at submillimeter to radio wavelengths. In fact, over 90% of the emergent luminosity of M17 is carried by photons with $\lambda \lesssim 100$ μm. We perform a spline interpolation (Fig. 3, *heavy line*) to the SED and integrate the result over all near-IR through radio wavelengths to obtain the total luminosity of the M17 complex,

$$L_{\mathrm{SED}}(d) = 4\pi d^2 \int F_\lambda\, d\lambda. \quad (6)$$

We determine the uncertainty on $L_{\mathrm{SED}}(d)$ by deriving maximum and minimum values using spline interpolations to the upper and

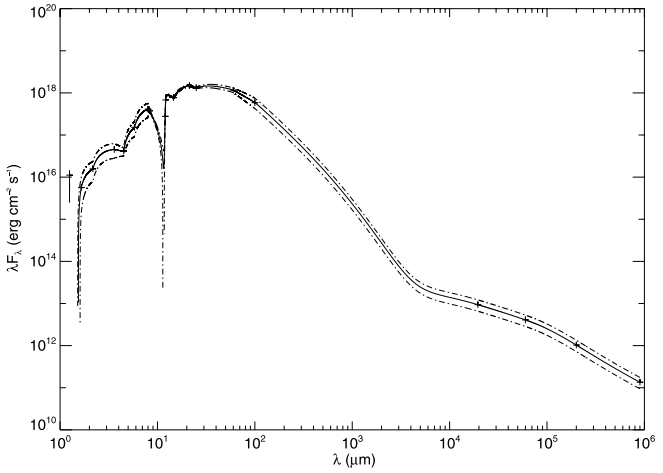

FIG. 3.— Global SED of M17 (aperture R4) plotted in λF_λ space. Over 90% of the emergent energy is carried by photons with $\lambda \lesssim 100$ μm. The solid curve is the spline interpolation of the SED that was integrated to obtain the total luminosity of M17, and the dash-dotted curves are the upper and lower uncertainty envelopes. The apparent deep absorption feature near 10 μm is an artifact of the spline interpolation. The large uncertainties on the *JHK*$_S$ flux values cause the interpolation to fail at the extreme short-wavelength end of this plot, but because the near-IR contributes a negligible amount of energy to the overall SED, this does not significantly impact the result of the integration.

lower error envelopes of F_λ shown in Figure 3 (*dash-dotted lines*). The often-cited (e.g., Chini et al. 1980) kinematic distance to M17 is 2.2 kpc, which gives $L_{\rm SED}(2.2\ {\rm kpc}) = 4.5 \pm 0.6 \times 10^6\ L_\odot$. More recent photometric distance estimates place M17 closer to the Sun, at 1.3 kpc (Hanson et al. 1997) or 1.6 kpc (Nielbock et al. 2001). Our derived luminosity is significantly reduced using a nearer distance estimate: $L_{\rm SED}(1.6\ {\rm kpc}) = 2.4 \pm 0.3 \times 10^6\ L_\odot$.

We compare the observed total luminosity of M17 to the combined bolometric luminosity of all the known ionizing stars in the NGC 6618 cluster. A similar analysis of the energetics of M17 was attempted by Harper et al. (1976) who derived a luminosity of $5.6 \times 10^6\ L_\odot$ and concluded that the region must contain the equivalent of 5–10 O5 stars. Currently there are 13 known O stars in NGC 6618. These are listed in order of decreasing mass in Table 3, along with their bolometric luminosities estimated from the calibrations of bolometric luminosity with spectral type of Martins et al. (2005). The cluster also contains at least 35 B stars earlier than B3 (see Appendix A of T03), and we include these in our energy calculations using the bolometric luminosities of de Jager & Nieuwenhuijzen (1987) but do not list them in Table 3 to save space. Because the spectral types of several of the O stars are poorly constrained, we are able only to give maximum and minimum possible values for the total bolometric luminosity of the ionizing stars, obtaining $L_{\rm OB}({\rm max}) = 3.58 \times 10^6\ L_\odot$ and $L_{\rm OB}({\rm min}) = 2.72 \times 10^6\ L_\odot$ for the combinations of all earliest and all latest possible spectral types, respectively. We assume that all of the stars are dwarfs on the zero-age main sequence (ZAMS); this is reasonable given the youth of the cluster (Jiang et al. 2002). Over 96% of the luminosity is produced by the 13 O stars alone, and virtually all of the remainder is accounted for by the early B stars. This is consistent with the ZAMS luminosity function of a cluster that obeys a Salpeter-type initial mass function; less than 1% of the total bolometric luminosity will come from stars later than B3.

Our analysis of the energetics of M17 is summarized in Table 4. Energy is input to the nebula largely by UV radiation from the ionizing stars, and this radiation is reprocessed by dust grains and reemitted as IR photons. If the nebular geometry were spherical (in other words, a completely embedded cluster), all of the stellar flux would be intercepted and the emergent luminosity, $L_{\rm SED}$, would be equal to the stellar luminosity, $L_{\rm OB}$ (first row of Table 4). The IR morphology of M17 shows that this is clearly not the case. The dominant morphological features of M17 are the two emission bars that meet each other at an apparent angle of 45°. Although the ionizing stars lie behind an average of $A_V = 8$ mag of optical extinction along the line of sight, the extinction in the direction of the opening angle between the bars is likely to be negligible. Several possible three-dimensional geometries are suggested by this morphology, and each would allow the nebula to intercept a fraction $f = 1 - \Omega/4\pi$ of the stellar flux, where Ω is the solid angle of the opening as measured from the cluster. In the most heavily embedded geometry, the bars are simply the cross-section of a cone that we view from the side. About 4% of the stellar flux escapes through the base of the cone, and the remaining $0.96 L_{\rm OB}$ is intercepted by the nebula and reprocessed to emerge in the SED. Alternatively, the geometry could take more of a "clamshell" form, where the two halves meet at an angle ranging from 45° ($f = 0.875$) if oriented edge-on to the line of sight, to perhaps 90° ($f = 0.75$) if inclined. This last configuration is the least embedded geometry that we can reasonably postulate for M17.

TABLE 3
LUMINOSITIES OF O STARS IN NGC 6618

Name[a]	R.A. (J2000.0)	Decl. (J2000.0)	Spectral Type	log $L_{\rm bol}$[b] ($L_\odot$)
CEN 1	18 20 29.92	−16 10 45.5	O4+O4	5.68+5.68[c]
CEN 43	18 20 33.14	−16 11 21.6	O3–O4	5.83–5.68
CEN 2	18 20 34.55	−16 10 12.1	O5	5.51
CEN 37	18 20 30.54	−16 10 53.3	O3–O6	5.83–5.30
OI 345	18 20 27.52	−16 13 31.8	O6	5.30
CEN 18	18 20 25.94	−16 08 32.3	O7–O8	5.10–4.90
CEN 25	18 20 30.92	−16 10 08.0	O7–O8	5.10–4.90
OI 352	18 20 35.86	−16 15 43.1	O8	4.90
CEN 16	18 20 22.76	−16 08 34.3	O9–B2	4.72–3.5
CEN 61	18 20 30.30	−16 10 35.2	O9–B2	4.72–3.5
CEN 3	18 20 35.47	−16 10 48.9	O9	4.72
CEN 31	18 20 24.45	−16 08 43.3	O9.5	4.62

NOTES.—Units of right ascension are hours, minutes, and seconds, and units of declination are degrees, arcminutes, and arcseconds.

[a] This list is adapted from Appendix A of T03 and Table 9 of Broos et al. (2006). Identifications are from the catalogs of CEN (Chini, Elsässer, & Neckel 1980) and OI (Ogura & Ishida 1976). Two sources from the T03 list, CEN 34 and CEN 102, have been dropped. These were not detected in X-rays, and their mid-IR colors suggest that they are either red giants not associated with M17 or YSOs, but not O stars.

[b] Bolometric luminosities are taken from Martins et al. (2005) for O stars and from de Jager & Nieuwenhuijzen (1987) for B stars.

[c] This source, Kleinmann's Anonymous Star, is a binary whose components are partially resolved by GLIMPSE.

A balancing of the possible combinations of input and the emergent energies compared in Table 4 reveals that M17 must lie at less than the kinematic distance of 2.2 kpc, because the maximum intercepted stellar luminosity falls below the minimum luminosity required to produce the observed SED at $d = 2.2$ kpc. We can place an upper limit on the distance to M17 by scaling the maximum stellar luminosity to the appropriate distance,

$$\frac{f L_{\rm OB}({\rm max})}{2.4 \times 10^6\ L_\odot} = \left[\frac{d({\rm max})}{1.6\ {\rm kpc}}\right]^2 .$$

This gives $d({\rm max}) = 1.9$ kpc for the conical geometry, $f = 0.96$. A similar argument yields a minimum distance $d({\rm min}) = 1.5$ kpc.

TABLE 4
Energy Budget of M17

Three-dimensional Nebular Geometry	Fraction of Flux Intercepted, f	fL_{OB}(max) ($10^6\ L_\odot$)	fL_{OB}(min) ($10^6\ L_\odot$)
Stellar Luminosity Intercepted by Nebula			
Spherical	1	3.58	2.72
Conical	0.96	3.44	2.61
Clamshell (45°)	0.875	3.13	2.38
Clamshell (90°)	0.75	2.68	2.04

d (kpc)	$L_{SED}(d)$ ($10^6\ L_\odot$)
Emergent Luminosity Observed in SED	
2.2	4.5 ± 0.6
1.6	2.4 ± 0.3

We therefore adopt the distance estimate of 1.6 kpc given by Nielbock et al. (2001). At this distance, the luminosity in the SED makes it unlikely that M17 contains any stars earlier than O4, although a spectral type of O3 for CEN 43 (see Table 3) is not ruled out.

We can constrain the most probable nebular geometry to some form between a cone and a clamshell with an opening angle of $\sim 45^\circ$. This interpretation agrees qualitatively with the structural model of Pellegrini et al. (2007) who deduce a similarly heavily embedded geometry for the M17 complex.

4. PAH EMISSION

The hypothesis that PAHs are responsible for a number of strong IR emission features was first proposed by Léger & Puget (1984) and has gained increasing support over the last 15 years (see Allamandola et al. 1989; Hudgins & Allamandola 1999; van Kerckhoven et al. 2000; Peeters et al. 2004). PAHs are large organic molecules incorporating tens or hundreds of C atoms. The C skeletal structure consists of linear chains or planar tessellations of multiple benzene rings with H atoms attached on the periphery (see Draine 2003 for a review). Exposure to UV radiation excites various vibrational modes in this class of molecules, causing them to radiate strongly as emission features in the IR. The major known emission features of PAHs are summarized in Table 5, along with the observational coverages of these features provided by the IRAC, *MSX*, and IRS SH data presented in this work.

While UV photons of sufficiently low energy excite PAH emission features, EUV and harder photons instead destroy the molecules (Voit 1992). Hard radiation fields are produced by OB stars, and the GLIMPSE images reveal that the mid-IR Galaxy is lit up by PAH emission that is particularly strong near H II regions like M17. The morphology of this emission often assumes ringlike "bubble" shapes, with sharp emission cutoffs surrounding cavities of little or no diffuse emission (Churchwell et al. 2006). The most likely explanation for the abrupt disappearance of PAH emission within H II regions is that the PAH molecules themselves are destroyed over a small distance scale or "edge" that lies near the I-front. The PAH molecules near this destruction edge are highly excited and emit strongly, and while this emission falls off rapidly with increasing distance beyond the I-front, it remains highly extended, stimulated by softer UV photons permeating the PDR.

4.1. *GLIMPSE Band-Ratio Images*

The GLIMPSE broadband mid-IR images of M17 do not show PAH emission alone, but rather a composite of emission features and dust continuum. It is possible, however, to locate

TABLE 5
Infrared Emission Features from PAH Molecules

Vibrational Mode[a]	λ (μm)	Observational Coverage
C-H stretching	3.3	IRAC 1
C-C stretching	6.2	IRAC 3
C-C stretching	7.7	IRAC 4, *MSX* A
C-H in-plane bending	8.6	IRAC 4, *MSX* A
C-H solo out-of-plane bending (PAH^+)[b]	11.0	*MSX* C, IRS SH
C-H solo out-of-plane bending	11.3	*MSX* C, IRS SH
C-H duo out-of-plane bending	12.0	*MSX* C, IRS SH
C-H trio out-of-plane bending	12.7	*MSX* C, IRS SH
C-H quartet out-of-plane bending	13.55	*MSX* D, IRS SH
C-C-C skeletal out-of-plane bending[c,d]	16.5, 17.4	IRS SH

[a] Except where noted otherwise, this list is based on Allamandola et al. (1989). "Solo," "duo," etc., refer to the number of H atoms contiguous with the H atom involved in the vibration.
[b] From Hudgins & Allamandola (1999).
[c] From van Kerckhoven et al. (2000).
[d] From Peeters et al. (2004).

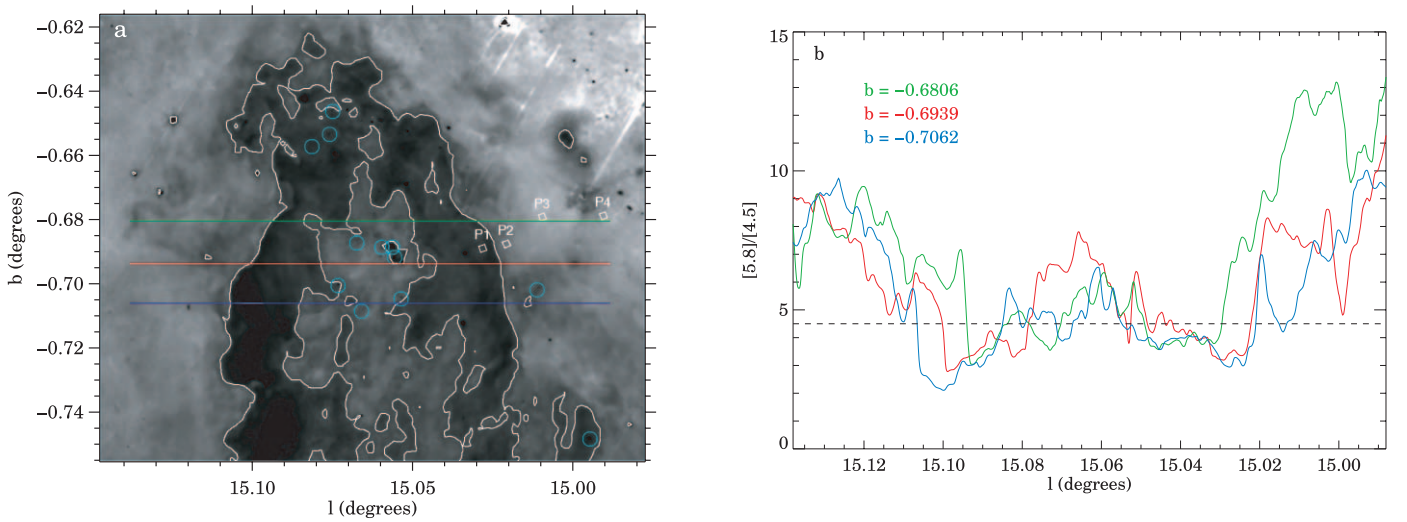

FIG. 4.—(*a*) Ratio image of IRAC [5.8]/[4.5]. The most prominent feature of this image is the dark region where PAH emission in IRAC [5.8] disappears. The boundary of this region can be traced by a fiducial contour (*white*) representing a ratio of [5.8]/[4.5] = 4.5. Four IRS SH slit pointings are overplotted, and one of them, P1, falls within the no-PAH zone. The positions of the O stars listed in Table 3 are indicated by cyan circles. Taking the band ratios in areas where the absolute mid-IR intensity is low amplifies image artifacts and noise. The bright area in the top right corner of this image takes a sight line through the molecular cloud M17 SW, where the extinction is particularly high, and hence some streaks (known artifacts of the [5.8] band) and speckling (noise) are apparent. (*b*) Image cuts in longitude *l* through the ratio image, color-coded by position in latitude *b*. All three cuts exhibit sharp dropoffs where they cross the outer boundary of the dark zone, and these transitions all span the fiducial contour value of 4.5 (*dashed line*).

the PAH destruction edge in the GLIMPSE images and thus to separate those areas of M17 that are PAH-dominated from those that are continuum-dominated. Because the IRAC [4.5] band does not contain any PAH feature, taking the ratio of this band with any of the other three bands largely divides out the continuum contribution, and the resultant band-ratio images trace primarily PAH emission. We produce these ratio images using background-subtracted GLIMPSE residual images from IRAC [3.6], [4.5], and [5.8]. We do not use IRAC [8.0] because it is saturated in much of the southern bar. We apply a median filter of width 7 pixels to the residual images to remove any remaining emission spikes from imperfectly extracted PSF wings of bright stars, and then smooth the result over three neighboring pixels using a boxcar algorithm.

Figure 4*a* shows the ratio image of IRAC [5.8]/[4.5] that traces the 6.2 μm PAH feature. The PAH-destruction zone, where the emission is continuum-dominated, appears as a prominent, dark Ω-shaped region. The outer boundary of this zone is the PAH destruction edge, and this can be traced by overlaying a single fiducial contour (Fig. 4*a*, *white*) representing [5.8]/[4.5] = 4.5. The outer boundary appears as a sharp dropoff, almost a step function, in three cuts taken through the ratio image (Fig. 4*b*), and this dropoff everywhere spans the fiducial contour value of 4.5. The inner boundary traced by this contour is more ragged, and the climb back above the fiducial contour is more gradual in the image cuts. The physical origin for this inner transition back to PAH-dominated emission is quite different from that of the PAH destruction edge. PAHs cannot survive at the heart of the M17 H II region, rather, the combined winds of the OB stars in the cluster have evacuated the central cavity of virtually all dust (T03; Pellegrini et al. 2007), thereby clearing out the source of the bright mid-IR continuum and leaving only the relatively faint signatures of the PAH-dominated front and back walls of the cavity. Figures 5*a* and 5*b* tell a similar story using the ratio image of IRAC [4.5]/[3.6] tracing the 3.3 μm PAH feature. Here the PAH-bearing band is divided into the PAH-free band, so the PAH destruction zone appears as a bright Ω instead of a dark one. The fiducial contour (Fig. 5*a*, *yellow*) has a value of [4.5]/[3.6] = 1.25 and traces almost the same path as the fiducial contour in Figure 4*a*.[14] In this combination of bands, the continuum-dominated region exhibits more structure. In particular, three probable stellar-wind bow shocks stand out in the northern bar. Two of these are associated with the late O stars CEN 16 and CEN 18 listed in Table 3, while the third is associated with an unidentified star in the northern bar. All of the bow shocks are oriented toward the central ring of O stars in NGC 6618. Among the bow shocks is one obvious dark pillar, or "elephant trunk," that also points toward the center of the ionizing cluster. These features provide further evidence for the importance of stellar winds in dynamically shaping the M17 complex (see T03).

As a control, we present the ratio image and corresponding cuts for IRAC [5.8]/[3.6], two PAH-bearing bands, in Figures 6*a* and 6*b*. The PAH destruction zone is less distinct in this ratio image and practically invisible in the one-dimensional cuts. The PAH destruction edge can be located as a thin, dark band in Figure 6*a*, highlighted by the overplotted fiducial contours from Figures 4*a* and 5*a* (*white and yellow*, respectively). The morphology of this ratio image may be attributed, in part, to the variation in the strength of the 3.3 and 6.2 μm PAH features relative to the respective continuum strengths in bands [3.6] and [5.8] along the PAH destruction edge. This interpretation implies that the 6.2 μm feature has a greater fractional contribution to the [5.8] band than the 3.3 μm to the [3.6] band. The appearance of the PAH destruction edge in this ratio image could also be influenced by differential extinction that affects the shorter wavelength IRAC bands more than the longer wavelength bands. The ratio of [5.8]/[3.6] increases with extinction because 3.6 μm photons are significantly more affected by extinction than 5.8 μm photons. If the extinction drops sharply just interior to the PAH destruction edge, the observed emission at 3.6 μm will recover

[14] We are primarily concerned here with the locations of these fiducial ratio contours, rather than the values of the fiducial ratios. Note that the ratios quoted in the text were derived from IRAC images without first applying the flux calibration correction factors described in § 3.1. With the correction applied, these ratios become [5.8]/[4.5] = 3.6 and [4.5]/[3.6] = 1.37.

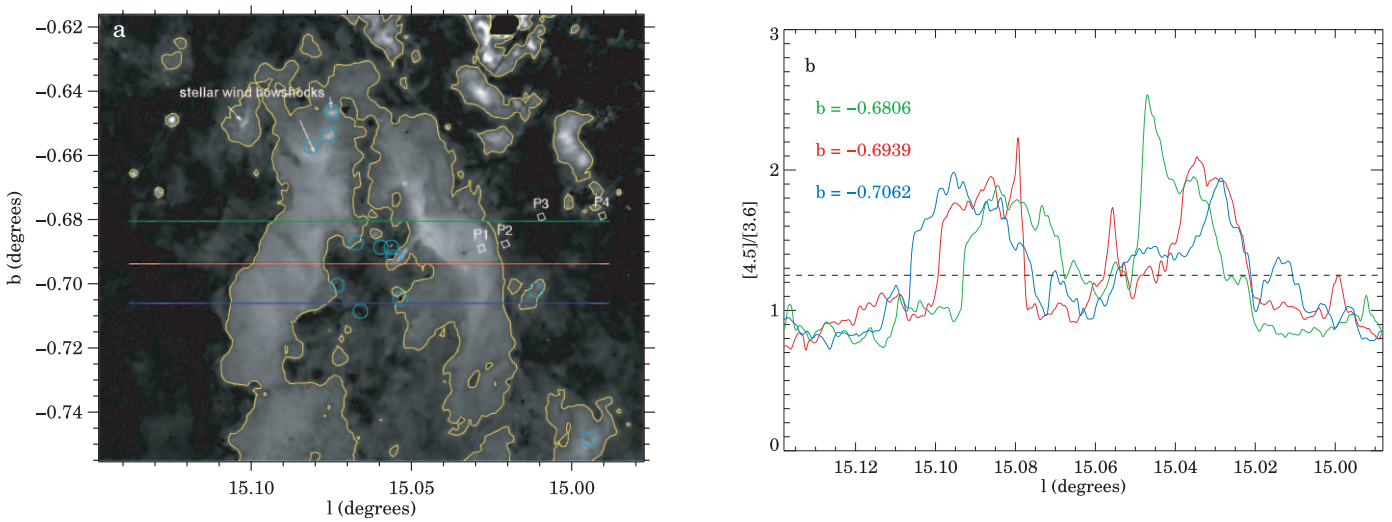

FIG. 5.—Same as Fig. 4, but taking the ratio of IRAC [4.5]/[3.6]. Because the band that has no PAH emission is divided by a PAH-bearing band, the no-PAH zone here appears as a bright region in the image. This region is bounded by the fiducial contour (*yellow*) [4.5]/[3.6] = 1.25. Note that the bright region highlights some distinct structures, including three bright apparent bow shocks associated with OB stars and a nearby dark pillar in the northern bar. The broad, bright ridge in the southern bar with a narrow finger jutting into the central cavity coincide with the brightest radio emission from the H II region (FCM84), hence these features may be due to enhancement of the Brα recombination line contribution to the [4.5] emission. The several bright structures in the top right corner that lie above the fiducial contour appear to be image artifacts in the [4.5] band.

more dramatically than the emission at 5.8 μm, suddenly suppressing the ratio. Conversely, the brightest area of this ratio image occurs in the top right of Figure 6*a*. This is the location of the molecular cloud M17 SW, where we would expect the highest extinction in this image.

We can apply the fiducial contours derived from the ratio images to the interpretation of the GLIMPSE mosaics. Single-band mosaics of M17 for each of the four IRAC bands are shown in Figure 7. The fiducial contour from Figure 4*a* is overplotted on the [4.5] and [8.0] images. The region exterior to this contour is PAH-dominated, while the Ω-shaped area enclosed by the contour is the PAH-free zone. The emission at [3.6], [5.8], and [8.0] increases sharply at the outer contour in both the northern and southern bars, evidence of the sudden appearance of the mid-IR PAH emission features. The dust continuum is particularly bright in the [8.0] band, hence this band shows a very bright ridge of emission in the southern bar interior to the PAH destruction edge. The [4.5] emission, in contrast, maintains approximately the same brightness across the PAH destruction edge, although some of the same dust continuum morphology exhibited by the [8.0] image is also readily apparent at [4.5]. Overplotted on the [3.6] and [5.8] images are contours of the 20 cm continuum from MAGPIS. The radio continuum traces free-free emission in the H II region, and these contours closely trace the [4.5] emission. This morphological similarity is due to the fact that the primary contributors to the IRAC [4.5] band are small-grain dust continuum photons with the $\sim$20% contribution from H I Brα recombination line emission estimated in § 3.2 above, both of which effectively trace the radio H II region. The strong PAH features in the other three IRAC bands contribute diffuse emission

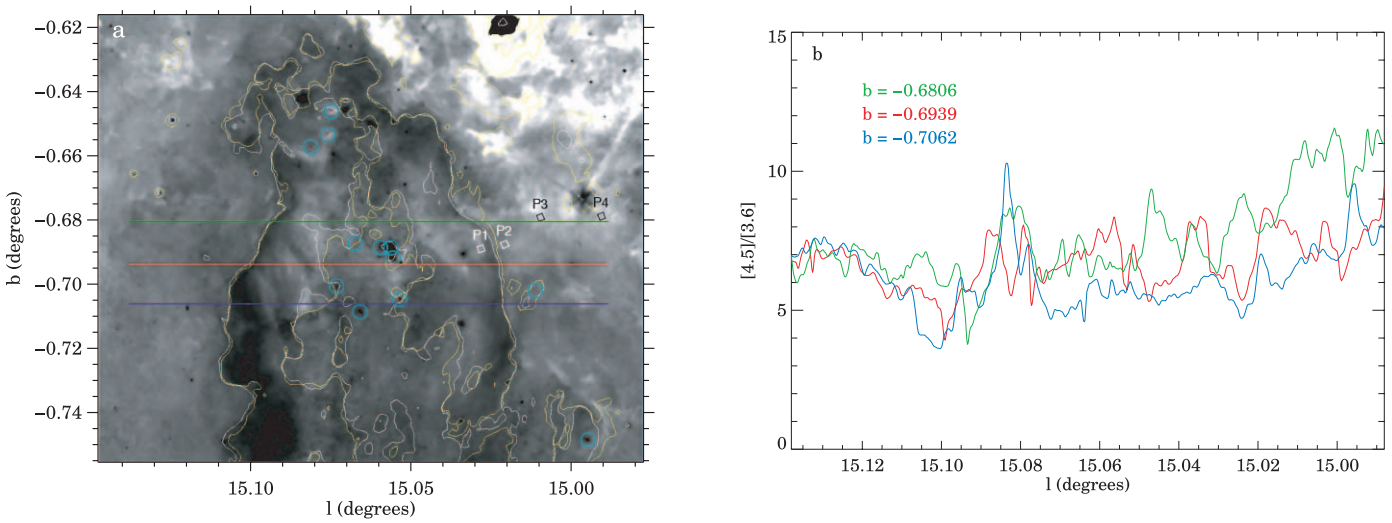

FIG. 6.—Same as Fig. 4, but taking the ratio of IRAC [5.8]/[3.6]. Because both bands include PAH emission features, the PAH destruction zone is much less distinct in this ratio image and practically invisible in its corresponding cuts. It is not possible to draw a single contour around the no-PAH zone based on the [5.8]/[3.6] ratio, however, the PAH destruction edge is visible in this image as a dark band with good spatial correspondence to the fiducial contours from Figs. 4*a* and 5*a* (*white and yellow*, respectively).

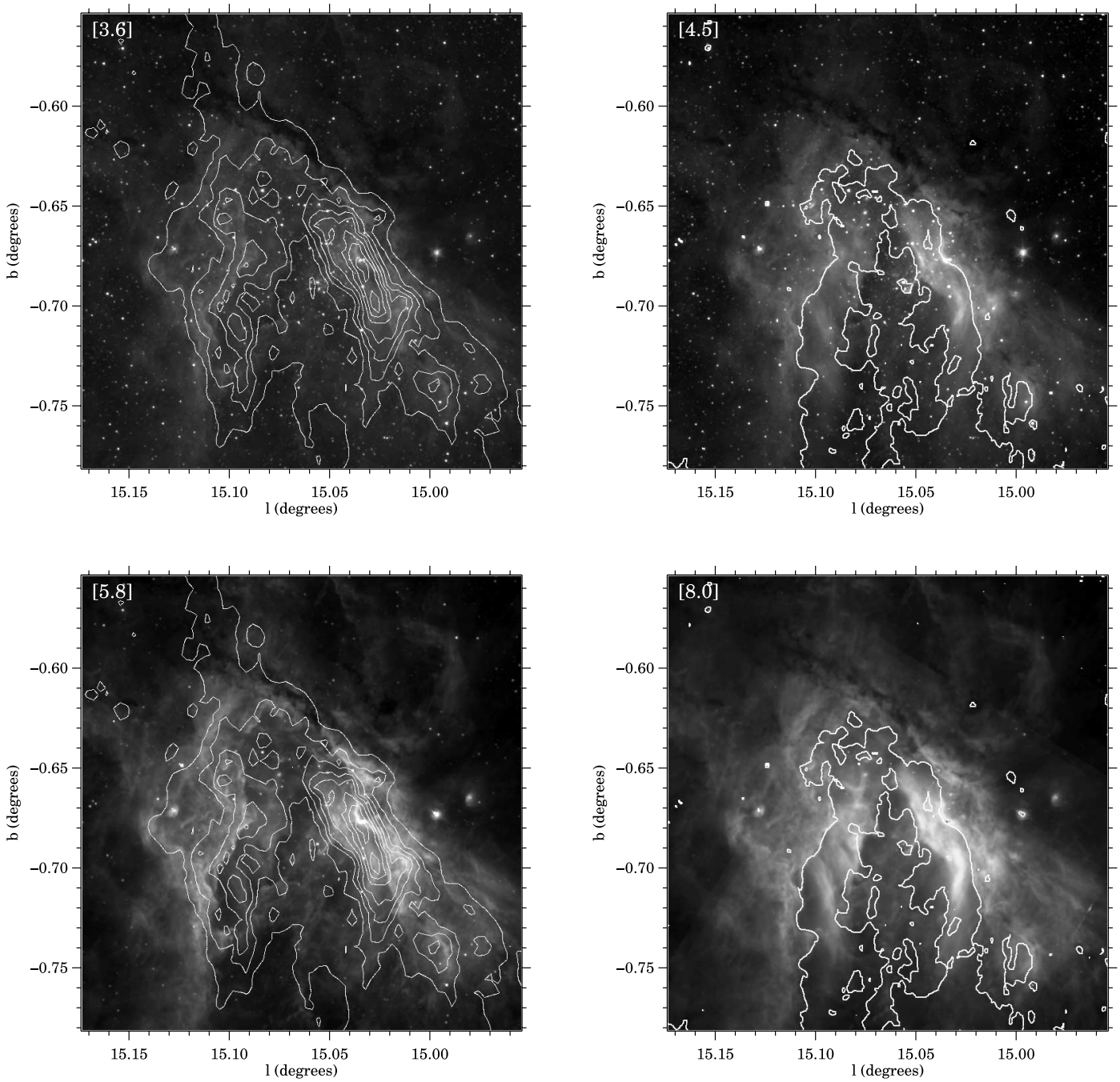

FIG. 7.—Comparison of the four GLIMPSE single-band mosaics of M17. All four images show the same field of view. IRAC [4.5] traces mainly dust continuum with a ~20% contribution from the H I Brα recombination line. The other three IRAC bands trace the same continuum but include a strong contribution from PAH emission features in the PDR. On the [4.5] and [8.0] images, the fiducial contour from Fig. 4 is shown tracing the PAH destruction edge and inner cavity wall. Overplotted on the [3.6] and [5.8] images are 20 cm VLA MAGPIS contours at intervals of 0.04 mJy beam^{-1} from 0.02 to 0.34 mJy beam^{-1}.

that remains relatively bright far into the PDR, yet most of the same morphological features are still faintly visible at [4.5]. This suggests that there may be some additional continuum contribution underlying all of the GLIMPSE bands, perhaps dehydrogenated PAHs as postulated by Giard et al. (1992) or the short-wavelength tail of the dust thermal continuum.

The structure of the PAH emission and location of the PAH destruction edge in M17 has been measured previously in both the northern (Chrysostomou et al. 1992) and southern (Giard et al. 1992; Crété et al. 1999; Kassis et al. 2002) bars. These observations were generally of lower resolution and sensitivity than the GLIMPSE data and covered only limited portions of the M17 complex, but the PAH morphologies presented agree well with our interpretation of the mid-IR morphology observed in GLIMPSE. A general picture emerges in which the PAH destruction edge occurs at or just outside the boundary of the H II region as defined by the I-front (FCM84), with the PAH emission extending far into the PDR. This is supported by the fact that the peak of the 20 cm emission is either coincident with or lies just inside the boundary of the PAH destruction zone throughout M17 (Fig. 7). It is difficult to precisely locate the position of the I-front relative to the PAH edge, owing to the complicated three-dimensional geometry of the region. The 20 cm emission appears to extend into the PAH-dominated PDR bars, but this is probably a projection effect.

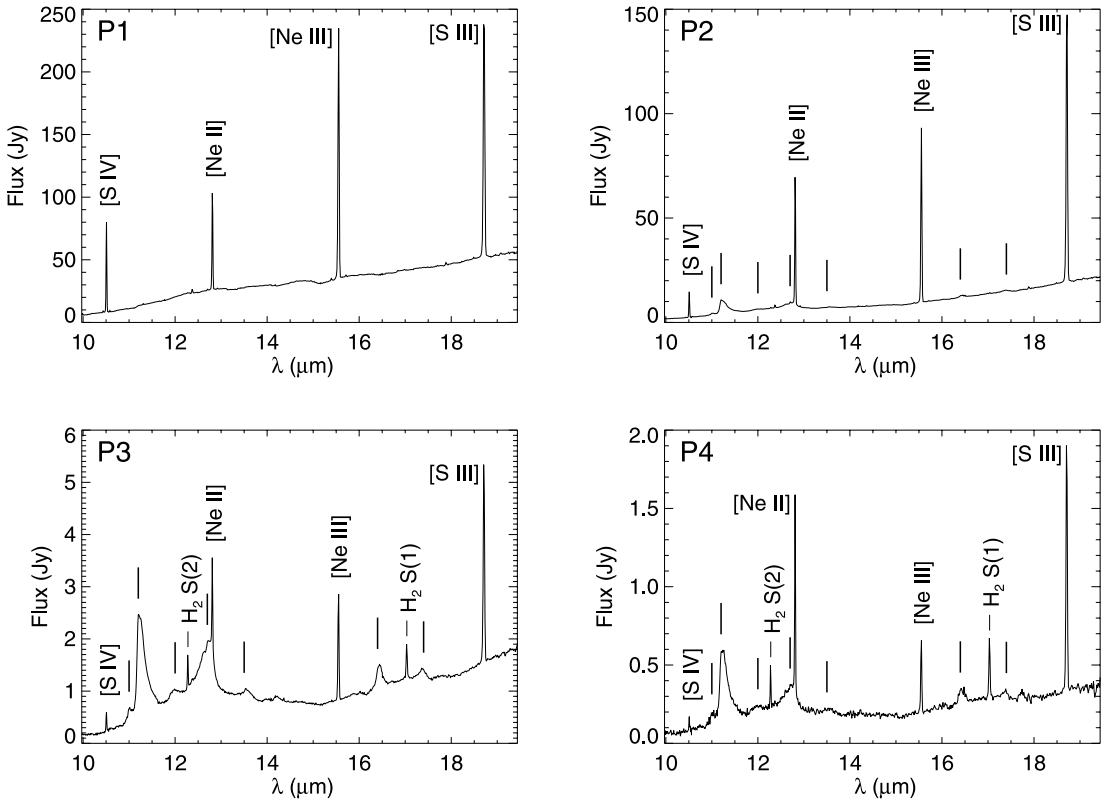

FIG. 8.—Four IRS SH spectra. The panels represent a series of slit pointings P1–P4 that span the H II region–PDR interface in the southern bar, in order of increasing distance from the ionizing cluster. Note the change in flux scale for each panel. The unlabeled vertical dashes mark PAH emission features listed in Table 5. There are no PAH features in pointing P1, the only pointing that falls inside the PAH destruction zone identified in Figs. 4–5. The changing physical conditions between the H II region and throughout the PDR are marked by the variation in relative strengths of the forbidden lines of different ionization states; both [S IV]/[S III] and [Ne III]/[Ne II] decrease monotonically from P1 to P4.

4.2. *IRS Spectroscopy*

To further test our results concerning the PAH emission, we analyzed a series of four spectra taken from the *Spitzer* IRS SH observations of the M17 southern bar. These four spectra were extracted from the slit pointings labeled P1–P4 in Figures 4*a*, 5*a*, and 6*a*. Only pointing P1 falls inside the PAH-destruction zone, and the other three pointings sample the PDR in order of increasing distance from the PAH destruction edge. The spectra from these four extractions, covering the IRS SH wavelength range of 9.9–19.6 μm, are plotted in the four panels of Figure 8. The brightness of the spectrum drops by over 2 orders of magnitude between pointings P1 and P4, and the flux scale has been adjusted accordingly in each panel. The PAH features listed in Table 5 that fall within this wavelength range are apparent in all but pointing P1; these are marked by vertical dashes but not labeled in order to minimize clutter in the plots. The disappearance of the PAH features in pointing P1 is fully consistent with our interpretation of the GLIMPSE images. In terms of absolute flux, the PAH emission features are the brightest by far in pointing P2, although this is not obvious due to the flux scaling required to display the full height of the bright fine-structure lines of [S IV] 10.510 μm, [Ne II] 12.814 μm, [Ne III] 15.555 μm, and [S III] 18.713 μm.

The fine-structure lines trace the ionization state of the gas in the PDR. Both the level of ionization in the gas and the strength of the emission lines are high near the I-front. Hence the ratio of the higher-ion lines, [S IV] and [Ne III], to their lower ion counterparts, [S III] and [Ne II], is greatest in extraction P1, the only one of our sample spectra taken from within the H II region. The brightness of the [S IV] line drops precipitously across the I-front/PDR interface, as a comparison of the P1 and P2 spectra shows. The ratios [S IV]/[S III] and [Ne III]/[Ne II] continue to decrease with increasing distance into the PDR, with the latter ratio inverting (becoming smaller than unity) somewhere between pointings P2 and P3. The overall diminishing of the fine-structure lines with distance from the ionizing cluster is consistent with the attenuation of the radiation field.

These same four spectra, normalized to their respective median continuum values, are plotted on the same set of axes in Figure 9*a*. A relative vertical shift of +1 is applied to each successive spectrum from P1–P4 for display purposes. The color-coding of the spectra corresponds to the colors (except that *white* maps to *black*) of the slit positions overlaid on the three-band (*red*: 5.8 μm; *green*: 4.5 μm; *blue*: 3.6 μm) GLIMPSE mosaic image of M17 in Figure 9*b*. The PAH destruction edge (Fig. 4, *white contour*) can be traced throughout this image where the [3.6] and [5.8] emission (*blue-red*) appears to give way to [4.5] emission (*green*). The O stars listed in Table 3 are identified (*cyan circles*), showing how the four IRS pointings together form a series of spectra sampling the southern bar at locations progressively more distant from the central ionizing cluster. Two bright infrared sources, the UC H II region M17-UC1 and the probable massive YSO M17 SW-IRS, are also labeled in Figure 9*b* for reference, but these sources are produced by B-type stars (FCM84), and hence are not significant contributors to the ionization of the M17 complex.

While the absolute strengths of the PAH features decrease with increasing distance into the PDR (Fig. 8), the strengths of the PAH features relative to the continuum increase, and the

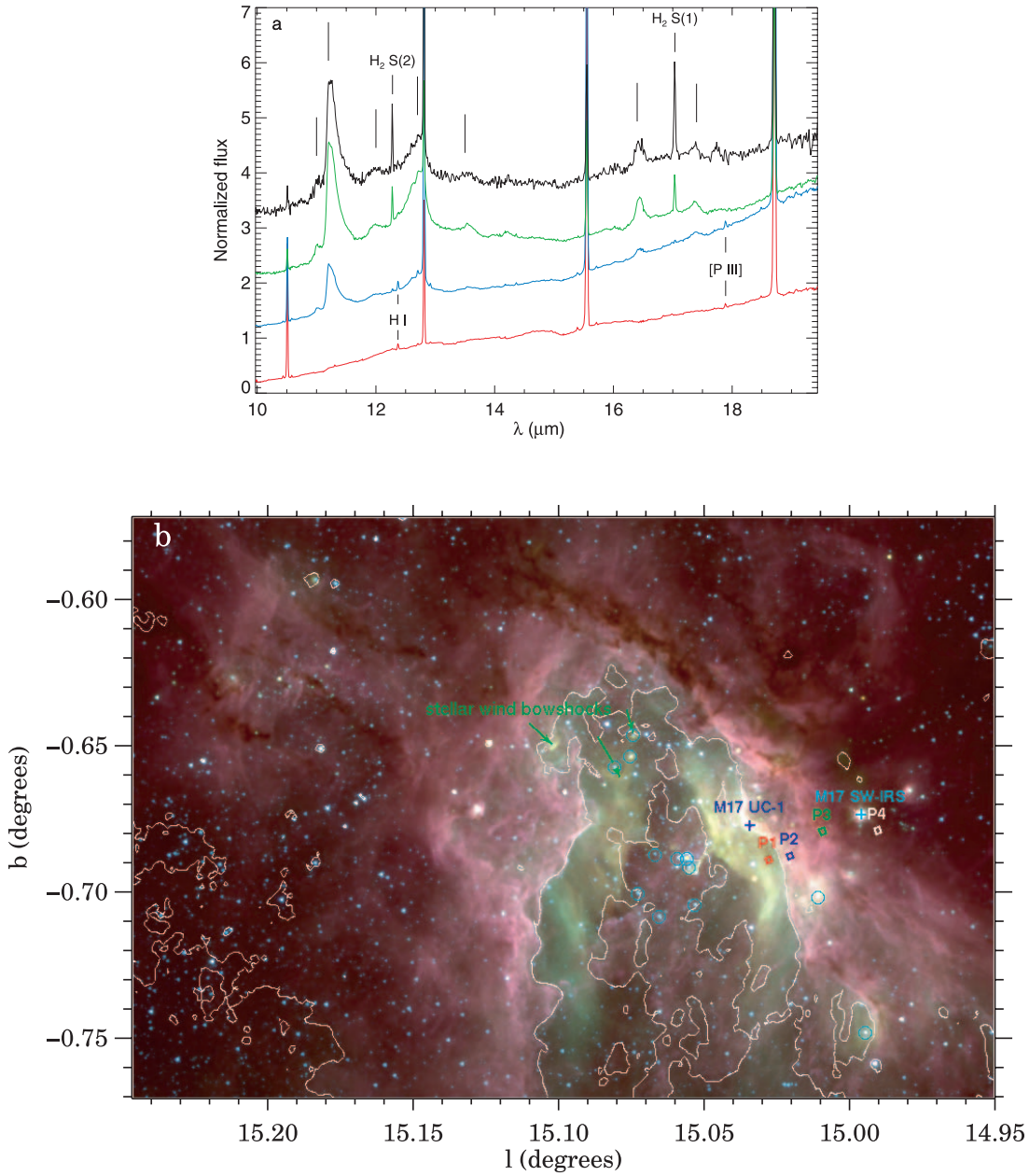

FIG. 9.—(*a*) Same four spectra as in Fig. 8, normalized to their respective median continuum values and plotted on the same scale. An arbitrary relative vertical shift of +1 is added to each successive spectrum for display purposes. This scaling displays the strengths of the PAH (*marked by unlabeled vertical dashes*) and H_2 emission features relative to the continuum at each position. The color-coding corresponds to that of the slit positions overlaid on the three-band (*red*: 5.8 μm, *green*: 4.5 μm, *blue*: 3.6 μm) GLIMPSE mosaic (*b*). The white fiducial contour from Fig. 4 is reproduced here. The O stars listed in Table 3 are marked by cyan circles. Green arrows point toward the upstream direction of the stellar-wind bow shocks. There is an elongated pillar near the largest bow shock with a bright YSO at its tip. The orientations of the arrows and the pillar converge on the central ring of O stars. Also labeled are the UC H II region M17-UC1 and the bright IR source M17 SW-IRS.

strengths of the molecular hydrogen lines, $H_2(0, 0)$ $S(1)$ at 12.279 μm and $H_2(0, 0)$ $S(2)$ at 17.035 μm, increase relative to the PAH emission. The shapes and relative strengths of the PAH features do not appear to change much between the spectra. This is puzzling, considering that we might expect at least the 11.0 μm feature, attributed to PAH cations (PAH^+) (Hudgins & Allamandola 1999) to lose strength relative to the neighboring strong PAH neutral feature at 11.3 μm with increasing distance into the PDR, as the overall level of ionization in the gas is observed to decrease.

The PAH emission is not confined to the strong features. Clearly apparent in the P2–P4 spectra in Figure 9*a* are broad emission plateaus extending from 11–14 μm and 16.5–17.5 μm (van Kerckhoven et al. 2000), connecting groups of PAH emission features that are related by vibrational mode (see Table 5). The relative strengths of the PAH emission features do not appear to vary much throughout the PDR, even as the overall brightness of the PAH emission spectrum decreases with increasing distance from the PAH destruction edge. This suggests that the PAH features in the IRAC bands, which fall shortward of the IRS SH wavelength coverage, should exhibit similar spatial morphologies. Follow-up observations of M17 using the IRS SL mode would enable an investigation of the shorter wavelength PAH features in more detail, but we can produce a rough morphological comparison using our available data.

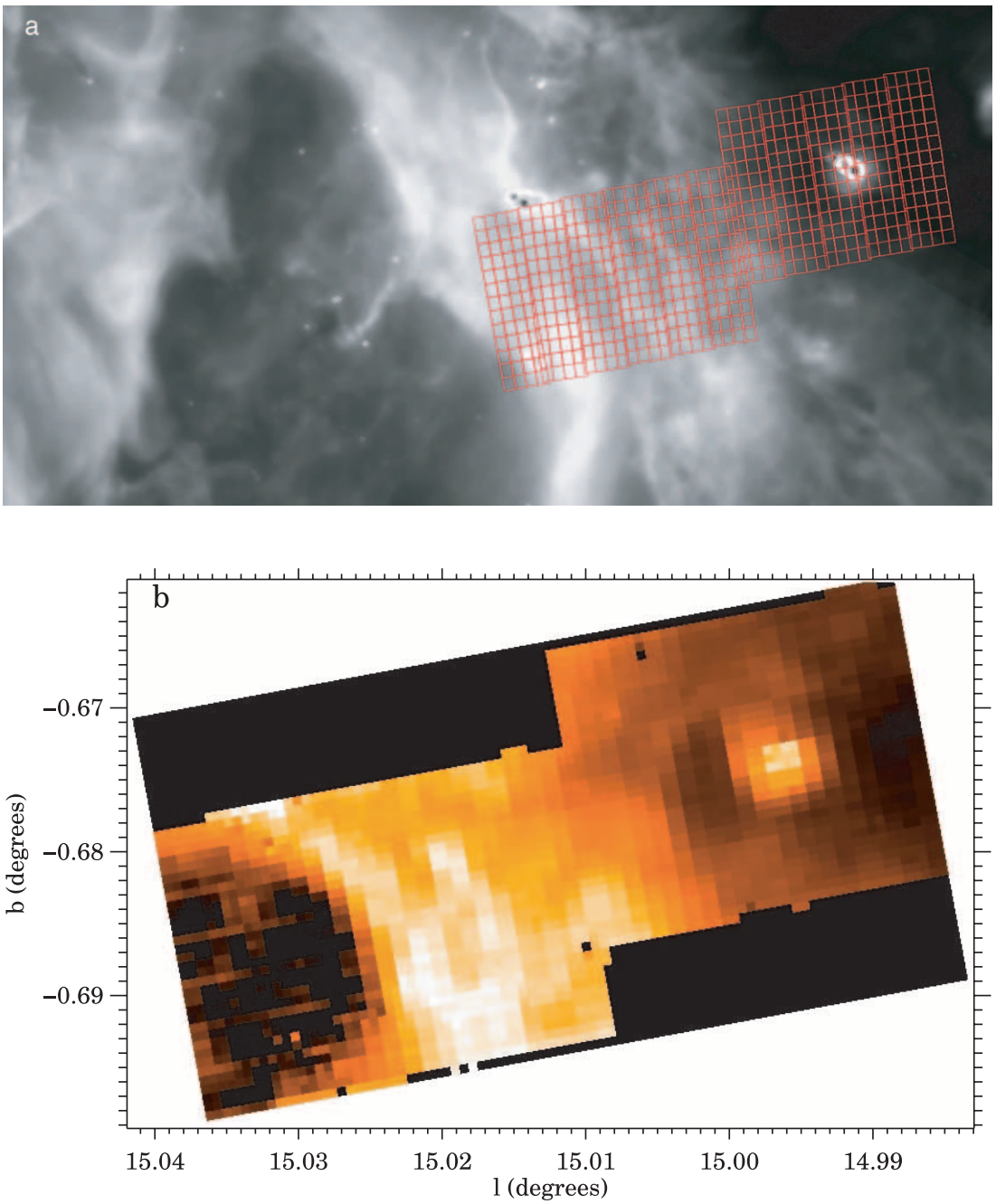

FIG. 10.—(*a*) Extraction boxes (*red*) used to create an IRS SH spectral map are overlaid on an IRAC [8.0] mosaic of M17. (*b*) Map of the 11.3 μm PAH feature, constructed from the IRS SH spectral map. The spatial resolution of the PAH map is lower than that of the IRAC [8.0] image by a factor of $\sim$10. Although the overall morphological similarities are unmistakable, there is one crucial difference between the PAH map and the [8.0] image. The PAH emission in the map disappears to the left of the bright arc of the PAH destruction edge, while bright continuum dominates the same part of the broadband image. M17 SW-IRS is visible in both panels as the bright point source at (l, b) = (14.996, −0.673).

We used CUBISM version 1.01 to produce a map of the 11.3 μm PAH feature from the IRS SH map. The extraction boxes for the spectral map are overlaid on an IRAC [8.0] image mosaic of M17 in Figure 10*a*, and the 11.3 μm PAH map is shown in Figure 10*b*. The map shows a narrow spectral window between 11.16 and 11.40 μm with adopted continuum regions at 10.80 to 10.92 μm and 11.67 to 11.80 μm. We avoid the 11.0 μm PAH emission feature for continuum subtraction. Note that CUBISM uses selected regions on either side of the feature to estimate the continuum. For broad features and a steep continuum, the subtraction is not perfect. Adopting different spectral regions for the continuum will yield minor variations in the map. Also note that the IRS SH module uses 2 pixels in the cross dispersion direction, and for our AORs (full steps perpendicular) the map necessarily contains 2 pixel spatial averages across the slit. If there are gaps in the maps, and CUBISM does not contain sufficient information to assign a value to a pixel, the software assigns a value of zero. This occurred in approximately 2% of the pixels, and to compensate we have simply interpolated a value from neighboring pixels.

Comparison of Figures 10*a* and 10*b* reveals similarities between the morphology of the 11.3 μm PAH emission feature

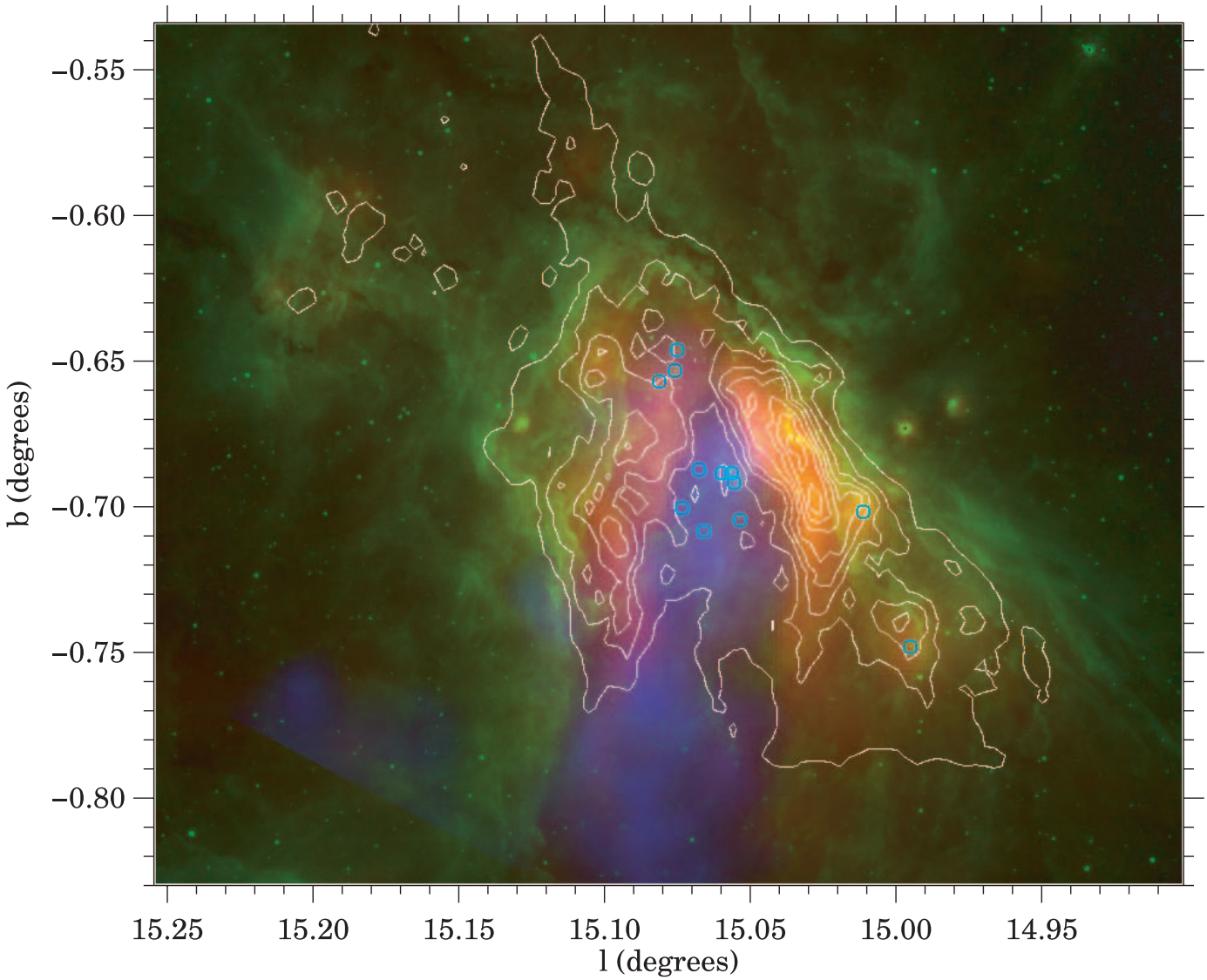

FIG. 11.—Multiwavelength M17. A river of MK plasma glows in soft X-rays (0.5–2.0 keV *Chandra* diffuse emission map from T03; *blue*) as it flows outward from the central cavity surrounding the O stars of NGC 6618 (*cyan circles*). The radio H II region (20 cm continuum; *white contours*) defines the cavity walls, and warm dust permeates the ionized gas, as shown by the 21.3 μm continuum emission (*MSX* E; *red*). The entire M17 complex is surrounded by a dusty wrapper (GLIMPSE [5.8]; *green*) that traces the PDR in emission from PAHs.

and the IRAC [8.0] broadband emission. The brightest emission in the 11.3 μm map occurs near the arc of the PAH destruction edge, to the left of which the emission drops to virtually zero. M17 SW-IRS is also prominent. Both the PAH destruction edge and M17 SW-IRS can be identified in the [8.0] image as well, but the former is more difficult to spot because of the sharply rising brightness of the 8.0 μm continuum inside the H II region. This highlights the major difference between the PAH spectral map and the IRAC [8.0] image; the brightest region of [8.0] in the entire M17 complex is almost pure continuum emission, devoid of PAHs. *Spitzer* IRAC images of energetic H II regions such as M17 should therefore not be interpreted solely in terms of PAH emission, because the continuum contribution can be strong, even dominant, especially at 8.0 μm.

4.3. *PAH Destruction by EUV and X-Ray Photons*

Figure 11 gives a multiwavelength view of M17. A hot plasma outflow from the cavity surrounding the ionizing star cluster glows in soft X-rays (*blue*) and the cavity walls are demarcated by 21.3 μm dust continuum emission (*red*). The entire M17 complex is surrounded by a PAH-emitting "wrapper" (*green*) that traces the boundary of the PDR. Whether the onset of PAH emission coincides precisely or only approximately with the boundary of the PDR is impossible to determine due to projection effects. In this section we show that the dearth of PAH emission inside the H II region is most likely due to destruction by stellar EUV photons. Given the X-ray content of M17 (T03) we also consider the role of X-rays in PAH destruction and in particular whether they are able to push the location of the PAH destruction edge beyond the I-front.

EUV and X-ray destruction of PAHs is governed by the processes of photothermodissociation (Léger et al. 1989) and Coulomb explosion (Leach 1987). Photothermodissociation is a process analogous to sublimation in which transient heating vibrationally excites PAHs. Coulomb explosion involves double photoionization. The resulting dication generates a repulsive force in excess of the potential barrier, thus fragmenting the PAH. Larger PAHs are destroyed more rapidly since they present greater

cross sections. The destruction rate a distance r from a source with luminosity spectrum L_E is

$$\Gamma_D = N_{\rm C} \int \frac{\sigma_E L_E}{4\pi r^2} e^{-\tau_E} \frac{dE}{E} \ \left({\rm s}^{-1}\right), \tag{7}$$

where $N_{\rm C}$ is the number of carbon atoms per PAH molecule (we use $N_{\rm C} = 100$ in our calculations), σ_E is the photoionization cross-section, and τ_E is the optical depth.

PAHs are able to rebuild by accreting carbon atoms. This accretion rate is given by Voit (1992) as

$$R_{\rm C^+} n({\rm C^+})(3.8 \times 10^{-11}) Y N_{\rm C}^{3/2} n({\rm C^+}) \ \left({\rm s}^{-1}\right) \tag{8}$$

where $n(\rm C^+)$ is the number density of $\rm C^+$ and Y is the sticking coefficient (assumed to be of order unity). For simplicity, we will assume that carbon is undepleted and singly ionized, and take C/H $\sim 4 \times 10^{-4}$ (Spitzer 1978). This leads to an upper limit on $R_{\rm C^+}$.

We assume the UV radiation field is dominated by the central 8 O stars of NGC 6618 (Table 3) and synthesize black body curves for each star based on its radius and effective temperature (Table 1 of Martins et al. 2005) using

$$F_\lambda d\lambda = \frac{2\pi hc^2 \lambda^{-5}}{ehc\lambda kT - 1} \left(\frac{R}{r}\right)^2 d\lambda, \tag{9}$$

where $(R/r)^2$ is the geometrical dilution factor. We first consider the destruction of PAHs throughout the entire H II region, assuming the (unrealistic) case of zero attenuation. Using the carbon photoionization cross-section of Verner et al. (1996) in equation (7), and integrating over the range 11.26 eV $< E <$ 291 eV, between the energy threshold for the liberation of a carbon L-shell electron and the maximum energy for which the cross-section is valid, we find the destruction rate exceeds the accretion rate for $r < 400(10^3/n_{\rm H})^{1/2}(10^2/N_{\rm C})^{1/4}$ pc from the cluster center. This demonstrates that the O stars in M17 emit more than enough UV to destroy the PAHs in their vicinity. The fact that the observed PAH destruction edge falls near the I-front, only $\sim$1 pc from the ionizing stars, is evidence that the EUV radiation field is significantly attenuated in the H II region.

We then evaluated the destruction rate outside the I-front. We assumed the UV spectrum truncates abruptly at 13.6 eV, held τ_E constant at $10^{-21} N_{\rm H}$ (Osterbrock & Ferland 2006), set $r = 1$ pc in equation (7), and solved for the column density at which PAH creation balances destruction. The result, $N \sim 1.2 \times 10^{22}$ cm^{-2} with $n_{\rm H} = 560$ cm^{-3} (Pellegrini et al. 2007), would imply that the PAH destruction edge lies several pc outside the I-front. This is inconsistent with the observations. The discrepancy could be explained by additional extinction, most likely due to dust within the H II region.

Finally, to consider the role of X-ray photons we used the X-ray photoionization cross-section of Voit (1991) in equation (7). We calculated the X-ray emission (Raymond & Smith 1977) assuming a gas in coronal equilibrium at $T \sim 7 \times 10^6$ K with a total luminosity $L \sim 9.5 \times 10^{33}$ ergs s^{-1} (T03). Setting r to 1 pc in equation (7), we compute a maximum Γ_D (zero attenuation) of $1.1 \times 10^{-14} N_{\rm C}$ s^{-1}. If $n_{\rm H} \sim 560$ cm^{-3} (Pellegrini et al. 2007) and $N_{\rm C} = 100$, equation (8) shows that the destruction rate never exceeds the accretion rate. This suggests that X-rays are not a significant destruction mechanism of PAHs in M17 and hence do not significantly affect the location of the PAH destruction edge. Since M17 is particularly luminous in X-rays, we can extend our conclusion to suggest that X-ray destruction of PAHs is not an important mechanism in any Galactic H II region. PAH destruction is caused by the action of EUV photons.

5. CONCLUSIONS

We have utilized images from multiple Galactic plane surveys spanning the near-IR to radio continuum wavelengths to construct the global SED of M17. The integrated flux in this SED gives a bolometric luminosity of $2.4 \times 10^6\ L_\odot$ at a luminosity distance of 1.6 kpc. This is consistent with the total bolometric luminosity of the known OB stellar content of NGC 6618, the ionizing cluster of the M17 H II region. Our upper limit of 1.9 kpc on the luminosity distance rules out the kinematic distance estimate of 2.2 kpc. Accepting the distance estimate of 1.6 kpc derived by Nielbock et al. (2001) and used by T03 and others, the earliest type star in M17 may be O3 V, but it is unlikely either that there is more than one star earlier than O4 V or that many O stars (or other high luminosity stars) remain undiscovered in M17. We can also constrain the three-dimensional geometry of M17 to a form between a cone and a clamshell with a 45° opening angle. The structural model of Pellegrini et al. (2007) the most detailed three-dimensional model of the M17 nebular geometry to date, is consistent with our results. The Pellegrini et al. (2007) model, however, concentrates on the line-of-sight through the southern bar, noting in particular the nearly edge-on orientation of the interface between the H II region and the PDR, but is less specific in describing the same structures in the northern bar. The GLIMPSE images show a sharp separation between the PAH-dominated PDR and the dust continuum-dominated H II region in the northern bar as well as in the southern bar. This indicates that the northern bar also presents a nearly edge-on view of the interface of the PDR with the H II region.

We have located the PAH destruction edge surrounding the M17 H II region using band-ratio images produced from the GLIMPSE residual images. We confirm the disappearance of PAHs within the destruction zone using spectroscopic data from *Spitzer* IRS. We calculate the photodestruction rate of PAHs by EUV photons and find that this destruction mechanism accounts for the absence of PAHs in the M17 H II region. Comparison of the GLIMPSE images with the MAGPIS 20 cm maps reveals that the PAH destruction edge lies everywhere close to the I-front. Due to the complicated three-dimensional structure of M17, it is difficult to tell whether the edge of the H II region and the onset of PAH emission in the PDR are always spatially coincident or if there can be a significant gap between the two. We explored the possibility of an X-ray destruction mechanism for PAH molecules that could push the destruction edge beyond the I-front, but found that the diffuse X-ray flux in M17 observed by T03 is insufficient to destroy PAHs faster than they can form. This result likely applies to nearly all Galactic H II regions, the majority of which are less energetic than M17.

The anatomy of a massive star-formation region is exemplified by M17. A cluster of massive stars provides sufficient Lyman continuum radiation to ionize the surrounding gas and destroy PAH molecules. The H II region is permeated by dust, probably with small grain sizes (Giard et al. 1992), and these warm grains produce a bright IR continuum. Although stochastic heating processes probably dominate the continuum at $\lambda \lesssim 10$ μm, the radiation field is sufficiently strong that small grains can achieve thermal equilibrium and radiate approximately as blackbodies at longer mid-IR wavelengths. This continuum peaks at wavelengths from 20–100 μm, and hence H II regions generally stand out in *MSX* and *Spitzer* MIPS images. Helou et al. (2004) carried out a *Spitzer* study of the spiral galaxy NGC 300 and found that IRAC [8.0] emission tends to highlight the rims of star formation regions, while MIPS 24 μm emission usually peaks interior to these rims. The view of M17 presented in Figure 11 tells a similar

story, where the 21.3 μm dust continuum emission (*red*) highlights the H II region bars (radio contours), while the 5.8 μm PAH-dominated emission (*green*) wraps around the entire complex and defines a sharp rim at the PAH destruction edge.

In very energetic regions like M17, the dust continuum can be very bright even at IRAC wavelengths, hence care should be used in interpreting the IRAC images of bright H II regions. Because 3 of the 4 IRAC bands trace similar emission processes (dust continuum + PAH emission features), the remaining band, [4.5], tends to stand out in multiband color composite images. This band contains several emission lines, predominantly the Brα recombination line in an H II region. It is tempting to interpret the IRAC [4.5] emission, appearing as a "green glow" interior to the bright emission rims defining the PAH destruction edge in Figure 9*b*, as perhaps an ionized flow that emits strongly in Brα evaporating off of the interior walls of a dust cavity. Such an evaporating flow was proposed by Weaver et al. (1977) but we have shown that the Brα line contributes only $\sim$20% of the broadband IRAC [4.5] emission in M17. While the [4.5] image does trace the H II region, and there is a marginally significant enhancement of Brα interior to the PAH destruction edge, the "green glow" in M17 and IRAC color mosaics of similar H II regions is primarily an artifact of the image stretch used to create the color composites. The [4.5] band, lacking PAH emission, tends to be much fainter in diffuse emission than the [5.8] and [8.0] bands, hence the [4.5] stretch is often brightened relative to that of the other bands for display purposes. The [5.8] and especially [8.0] bands can exhibit bright continuum emission where there is no PAH contribution, hence in M17 there are two prominent diffuse emission edges, the outer edge of PAH destruction, and the inner edge closer to the ionizing cluster where the dust has been cleared away by stellar winds.

The dynamical effect of the combined OB stellar winds shapes the physical distribution of gas and dust in M17, as evidenced by the central cavity filled with shock-heated plasma and the apparent bow shocks near 4 massive stars. The PAH destruction edge has, in many places, a morphology suggestive of multiple shock fronts. The observed IR morphology of the region is further determined by the radiative effects of dust heating and PAH excitation. The results of this work provide further proof of the dominant feedback mechanisms employed by OB stars in shaping and illuminating their birthplaces.

We thank Leisa Townsley for providing us with images of the diffuse X-ray flux of M17 detected by *Chandra* and for her numerous helpful suggestions as the referee. We are grateful to Martin Cohen for his invaluable insights on diffuse flux calibrations. Discussions with Melvin Hoare provided useful ideas for improving this work. Support for this work, part of the *Spitzer Space Telescope* Legacy Science Program, was provided by NASA through contracts 1224653 (University of Wisconsin at Madison), 1224681 (University of Maryland), and 1224988 (Space Science Institute). J. M. S. was supported by NASA ATP grant NNGO5IGO9G. Additional support for *Spitzer Space Telescope* GO observations was provided by NASA through an award issued by the Jet Propulsion Laboratory (JPL) at the California Institute of Technology. M. G. W. was supported in part by NASA Long Term Space Astrophysics grant NNG05GD64G.

REFERENCES

Allamandola, L. J., Tielens, A. G. G. M., & Barker, J. R. 1989, ApJS, 71, 733
Altenhoff, W. J., Downes, D., Goad, L., Maxwell, A., & Rinehart, R. 1970, A&AS, 1, 319
Beichman, C. A., Neugebauer, G., Habing, H. J., Clegg, P. E., & Chester, T. J., ed. 1988, IRAS Catalogs and Atlases: Explanatory Supplement (NASA RP-1190; Washington: GPO)
Benjamin, R. A., et al. 2003, PASP, 115, 953
Broos, P. S., et al. 2006, ApJ, submitted (astro-ph/0612590)
Capriotti, E. R., & Kozminski, J. F. 2001, PASP, 113, 677
Carey, S. J., et al. 2006, BAAS, 209.8801
Chini, R., Elsässer, H., & Neckel, T. 1980, A&A, 91, 186
Chrysostomou, A., Brand, P. W. J. L., Burton, M. G., & Moorhouse, A. 1992, MNRAS, 256, 528
Churchwell, E., Wolfire, M. G., & Wood, D. O. S. 1990, ApJ, 354, 247
Churchwell, E., et al. 2006, ApJ, 649, 759
Cohen, M., et al. 2007, MNRAS, 374, 979
Conti, P. S., & Crowther, P. A. 2004, MNRAS, 355, 899
Crété, E., Giard, M., Joblin, C., Vauglin, I., Léger, A., & Rouan, D. 1999, A&A, 352, 277
de Jager, C., & Nieuwenhuijzen, H. 1987, A&A, 177, 217
Downes, D., Wilson, T. L., Bieging, J., & Wink, J. 1980, A&AS, 40, 379
Draine, B. T. 2003, ARA&A, 41, 241
Elmegreen, B. G., & Lada, C. J. 1976, AJ, 81, 1089
Fazio, G. G., et al. 2004, ApJS, 154, 10
Felli, M., Churchwell, E., & Massi, M. 1984, A&A, 136, 53 (FCM84)
Giard, M., Bernard, J. P., & Dennefield, M. 1992, A&A, 264, 610
Goss, W. M., & Shaver, P. A. 1970, Australian J. Phys. Astrophys. Suppl., 14, 1
Hanson, M. M., Howarth, I. D., & Conti, P. S. 1997, ApJ, 489, 698
Harper, D. A., Low, F. J., Rieke, G. H., & Thronson, H. A. 1976, ApJ, 205, 136
Hauser, M. G., et al. 1991, in AIP Conf. Ser. 222, After the First Three Minutes, ed. S. Holt & C. L. Bennett (New York: AIP), 161
Helfand, D. J., Becker, R. L., Fallon, A., & Tuttle, S. 2006, AJ, 131, 2525
Helou et al. 2004, ApJS, 154, 253
Houck, J. R., et al. 2004, Proc. SPIE, 5487, 62
Hudgins, D. M., & Allamandola, L. J. 1999, ApJ, 516, L41
Jiang, Z., et al. 2002, ApJ, 577, 245
Kassis, M., Deutsch, L. K., Campbell, M. F., Hora, J. L., Fazio, G. F., & Hoffman, W. F. 2002, AJ, 124, 1636
Kleinmann, D. E., & Wright, E. L. 1973, ApJ, 185, L131
Koo, B.-C., & McKee, C. F. 1992, ApJ, 388, 103
Lada, C. 1976, ApJS, 32, 603
Lada, C. J., DePoy, D. L., Merrill, K. M., & Gatley, I. 1991, ApJ, 374, 533
Leach, S. 1987, J. Electr. Spectrosc. 41, 427
Léger, A., Boissel, P., Désert, F. X., & d'Hendecourt, L. 1989, A&A, 213, 351
Léger, A., & Puget, J. L. 1984, A&A, 137, L5
Martins, F., Schaerer, D., & Hillier, D. J. 2005, A&A, 436, 1049
Meixner, M., Haas, M. R., Tielens, A. G. G. M., Erickson, E. F., & Werner, M. 1992, ApJ, 390, 499
Nielbock, M., Chini, R., Jütte, M., & Manthey, E. 2001, A&A, 377, 273
Ogura, K., & Ishida, K. 1976, PASJ, 28, 35
Osterbrock, D. E., & Ferland, G. J. 2006, Astrophysics of Gaseous Nebulae and Active Galactic Nuclei (Mill Valley: University Science Books)
Peeters, E., Mattioda, A. L., Hudgins, D. M., & Allamandola, L. J. 2004, ApJ, 617, L65
Pellegrini, E. W., et al. 2007, ApJ, in press (astro-ph/0611808)
Price, S. D., Egan, M. P., Carey, S. J., Mizuno, D. R., & Kuchar, T. A. 2001, AJ, 121, 2819
Price, S. D., Paxson, C., Engelke, C., & Murdock, T. L. 2004, AJ, 128, 889
Raymond, J. C., & Smith, B. W. 1977, ApJS, 35, 419
Schraml, J., & Mezger, P. G. 1969, ApJ, 156, 269
Skrutskie, M. F., et al. 2006, AJ, 131, 1163
Spitzer, L. 1978, Physical Processes in the Interstellar Medium (New York: Wiley)
Stetson, P. 1987, PASP, 99, 191
Subrahmanyan, R., & Goss, W. M. 1996, MNRAS, 281, 239
Townsley, L. K., Feigelson, E. D., Montmerle, T., Broos, P. S., Chu, Y.-H., & Garmire, G. P. 2003, ApJ, 593, 874 (T03)
Tsivilev, A. P., & Krasnov, V. V. 1999, Astron. Rep., 43, 511
van Kerckhoven, C., et al. 2000, A&A, 357, 1013
Verner, D. A., Ferland, G. J., Korista, K. T., & Yakolev, D. G. 1996, ApJ, 465, 487
Vig, S., Ghosh, S. K., Kulkarni, V. K., Ojha, D. K., & Verma, R. P. 2006, ApJ, 637, 400
Voit, G. M. 1991, ApJ, 379, 122
———. 1992, MNRAS, 258, 841
Weaver, R., McCray, R., Castor, J., Shapiro, P., & Moore, R. 1977, ApJ, 218, 377